A Modular Framework for Task-Agnostic, Energy Shaping Control of Lower-Limb Exoskeletons

Jianping Lin, Member, IEEE, Gray C. Thomas, Member, IEEE, Nikhil V. Divekar, Student Member, IEEE, Vamsi Peddinti, Robert D. Gregg, Senior Member, IEEE

Abstract-Various backdrivable lower-limb exoskeletons have demonstrated the electromechanical capability to assist volitional motions of able-bodied users and people with mild to moderate gait disorders, but there does not exist a control framework that can be deployed on any joint(s) to assist any activity of daily life in a provably stable manner. This paper presents the modular, multi-task optimal energy shaping (M-TOES) framework, which uses a convex, data-driven optimization to train an analytical control model to instantaneously determine assistive joint torques across activities for any lower-limb exoskeleton joint configuration. The presented modular energy basis is sufficiently descriptive to fit normative human joint torques (given normative feedback from signals available to a given joint configuration) across sit-stand transitions, stair ascent/descent, ramp ascent/descent, and level walking at different speeds. We evaluated controllers for four joint configurations (unilateral/bilateral, hip/knee) of the modular M-BLUE exoskeleton on eight able-bodied users navigating a multi-activity circuit. The two unilateral conditions significantly lowered overall muscle activation across all tasks and subjects (p < 0.001). In contrast, bilateral configurations had a minimal impact, possibly attributable to device weight and physical constraints.

Index Terms-Robotics, optimization, passivity-based control.

I. Introduction

E XOSKELETONS on the market today in rehabilitation applications, such as the ReWalk Personal [1] and Wandercraft Atalante X [2], provide complete assistance with highly-geared actuators that track pre-defined reference trajectories. While these designs are appropriate for severe impairments like paraplegia, they hinder users from populations

This work was supported by the National Institute of Biomedical Imaging and Bioengineering of the NIH under Award Number R01EB031166 and by the National Science Foundation under Award Number 1949869. The content is solely the responsibility of the authors and does not necessarily represent the official views of the NIH or NSF.

Jianping Lin is with the State Key Laboratory of Mechanical System and Vibration, School of Mechanical Engineering, Shanghai Jiao Tong University, Shanghai 200240, China. He was with the Department of Robotics, University of Michigan, Ann Arbor, MI 48109, USA (Email: jplin@ieee.org).

Gray C. Thomas is with the Department of Mechanical Engineering, Texas A&M University, College Station, TX 77843, USA. He was with the Department of Robotics, University of Michigan, Ann Arbor, MI 48109, USA (Email: gthomas@tamu.edu).

Nikhil V. Divekar is with the Department of Robotics, University of Michigan, Ann Arbor, MI 48109, USA (Email: ndivekar@umich.edu).

Vamsi Peddinti is with the Department of Electrical and Computer Engineering, University of Michigan, Ann Arbor, MI 48109, USA (Email: vamsi.speddinti@gmail.com).

Robert D. Gregg (Corresponding Author) is with the Department of Robotics, University of Michigan, Ann Arbor, MI 48109, USA (Email: rdgregg@umich.edu).

with full or remnant volitional control over their limbs. Highly-geared actuators introduce high mechanical impedance at the joint and therefore impede the operator's ability to move the device under their own power (i.e., backdrive the actuators). Although these actuators can still achieve normative joint motions through position control methods for a variety of tasks [3], [4], these predefined patterns inevitably conflict with the user's desired motion. Thus, the conventional actuation and control approach for exoskeletons has recently given way to alternative approaches for assisting remnant voluntary ability.

Low-impedance actuation systems [5], such as quasi-directdrive actuators [6]-[10] and series elastic actuators [11]-[14], are enabling a paradigm shift from task-specific, position control to task-agnostic, torque control approaches that deliver partial rather than complete assistance to the user. These backdrivable designs allow augmentation of voluntary human motion [8], [15], compensation for human-exoskeleton mass/inertia [16], [17], and direct amplification of human strength [18]. Our group recently developed an open-source hardware platform called the modular backdrivable lower-limb unloading exoskeleton (M-BLUE) [10], which exemplifies the field's trend toward lighter, minimalist structures for attaching quasi-direct drive actuators to people. As backdrivable exoskeleton designs become increasingly capable and versatile, there arises a greater need for generalizable control methods that operate reliably across the core activities of daily life, allow for adjustment of the control behavior, avoid instability, and can be deployed on different lower-limb joint configurations (such as the hip and/or knee of the *M-BLUE* system).

Machine learning with human biomechanical data has enabled several control approaches for backdrivable exoskeletons with varying degrees of generalizability. For example, a recurrent neural network enabled stair climbing with a knee exoskeleton in [19] but did not consider other activities. Deep learning has been used to directly estimate biological hip moments consistently across multiple activities without explicitly detecting the activity (making it task-agnostic), but this method required extensive device-specific training data [20]. The gait analysis field has similarly investigated methods to estimate joint torques and ground reaction forces from inertial sensors [21]. While neural networks can estimate continuous gait phase to control the timing of a predefined assistive torque profile [22], [23], secondary task classifiers [24] are typically required to adapt assistance appropriately between tasks. Generally speaking, these black-box strategies based on machine learning offer no guarantees of safety and stability, especially outside the training dataset, requiring extensive training and validation for every exoskeleton application.

Analytical alternatives to learning approaches include phase estimators, which determine the timing for pre-defined torque profiles. However, model-based phase estimators are currently limited to walking [25] or a continuum of ramp walking tasks [26]. The latter case demonstrated the potential to track both phase and task variables (like stride length and ground incline) in order to apply task-appropriate ankle torque, but applications have been limited to a narrow set of periodic walking behaviors. A model-free alternative, adaptive oscillators [27], [28] offer the ability to track any periodic task with provable convergence properties. However, the periodicity assumption limits non-steady-state tasks outside of the laboratory [29], and adaptive oscillators cannot automatically adapt the torque profile to be task-appropriate. Despite having analytical guarantees, these methods do not sufficiently generalize across activities to seamlessly augment voluntary human motion.

Another analytical control method known as *energy shaping* augments the plant dynamics to correspond to a new system Lagrangian (or, equivalently, Hamiltonian) energy function when the loop is closed [30], [31]. Considering the humanexoskeleton system as the plant, energy-shaping controllers provide assistive torques that augment the user's perceived dynamics while they remain in control of their joint kinematics [6], [32], [33]. However, underactuated systems like lowerlimb exoskeletons can only achieve closed-loop dynamics that satisfy a set of nonlinear partial differential equations called the *matching conditions*, which determine the achievable form of the closed-loop system's energy and the existence of a corresponding feedback law. Our prior works derived solutions to the matching conditions for exoskeletons of increasing complexity, starting from a unilateral ankle-only system [34], and advancing through a unilateral ankle-knee system in several stages: first handling known [35] or unknown [36] ground-contact conditions, then adding passive velocity feedback [32], ground reaction force feedback [37], and global angle information [33]. This last approach was also extended to a bilateral hip exoskeleton with a unified stance/swing controller [38]. Each additional feature necessitated restructuring the matching conditions and the parameterization of target energies to satisfy these conditions. The most recent of these methods reshape a port-Hamiltonian representation of the dynamics according to the theory of interconnection and damping assignment passivity-based control (IDA-PBC) [39], [40]. While potential-energy-shaping methods can be designed intuitively, e.g., through gravity compensation [35] or virtual model control [41], the complex energy targets needed for task-agnostic biological torque estimation are better suited to being optimized across multi-activity able-bodied datasets [32], [33], [38]. While these methods successfully generalized across activities, their matching conditions were limited to specific joint configurations.

To facilitate wide deployment across backdrivable exoskeletons, the latest energy shaping framework in [33] must be further generalized to optimize task-agnostic energy shapes for arbitrary lower-limb joint configurations. Because the prior solution to the matching conditions is unique to exoskeletons at the beginning or end of a leg's kinematic chain, the framework in [33] cannot be implemented on many of the unilateral or bilateral joint configurations of *M-BLUE*. In addition, this controller was designed to switch discretely when contact with the ground is detected, which makes it difficult to handle the multi-contact scenarios in bilateral exoskeleton configurations. Other limitations of [33] include a fully centralized controller that cannot facilitate distributed computation across bilateral knee configurations, a lack of adjustability in situations where user feedback directly contradicts the dataset's prescribed human torque, and an optimization that requires generic solvers rather than computationally efficient convex optimization.

This paper addresses the above limitations through a generalized, modular version of the multi-task optimized energy shaping (M-TOES) framework that can be readily deployed on the different joint configurations of M-BLUE and other exoskeletons. The contributions of this paper are summarized as follows. First, we extend our previous port-Hamiltonian control method [33] by adding the key features of modular energy bases, convex penalties on incorrect torque sign, and unification of stance and swing controllers by use of insole force sensors. A convex, data-driven optimization trains an analytical control model to instantaneously estimate assistive joint torques across multiple activities for any lower-limb joint configuration. The presented modular energy basis is sufficiently descriptive to fit normative human joint torques (given normative feedback from signals available to a given joint configuration) across sit-stand transitions, stair ascent/descent, ramp ascent/descent, and level walking at different speeds. Second, we rigorously analyze the behavior of the target energy resulting from these controllers, including all possible power leaks due to practical relaxations of the matching conditions and passivity (introducing two additional sources of power leak beyond [33]). Third, we deploy the modular control method on four different configurations of the M-BLUE system (unilateral hip, bilateral hip, unilateral knee, and bilateral knee), demonstrating stability, task flexibility, and muscle effort reductions with N=8 able-bodied participants performing the primary activities of daily life.

II. MODULAR, MULTI-TASK OPTIMIZED ENERGY SHAPING (M-TOES)

This section introduces our lower-body sagittal-plane model of the human-exoskeleton system using a port-Hamiltonian formulation, and revisits interconnection and damping assignment passivity-based control (IDA-PBC) in the context of the ipsilateral leg of the model. We proceed by coupling the two legs together, enabling the consideration of energy shaping for the entire model, and accommodating various configurations of assisted joints and available sensors. We offer a modular solution to the matching conditions, taking into account contact constraints. Additionally, we define an optimization that will efficiently produce the corresponding multi-task control law for each possible configuration. Fig. 1 provides a visual summary of the overall design process, illustrating the ultimate feedback loop within our proposed human-exoskeleton system.

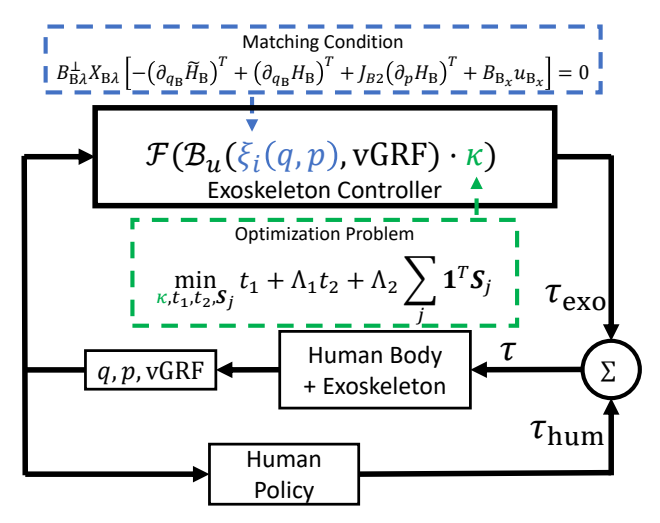


Fig. 1. Diagram of the control design process leading to the ultimate feedback loop of a human leg wearing an energy-shaping exoskeleton. Here, τ_{hum} represents the total human input, τ_{exo} represents the exoskeleton input, $\tau = \tau_{\text{hum}} + \tau_{\text{exo}}$ represents the combined human-exoskeleton input, and q, p, and vGRF correspond to generalized coordinates, conjugate momenta, and vertical ground reaction force, respectively. The input of the exoskeleton controller includes basis functions ξ_i satisfying the *matching condition* (Section II-C) and linear coefficients κ_i returned by the optimization problem (Section II-F). The exoskeleton controller operates without human intent or task recognition.

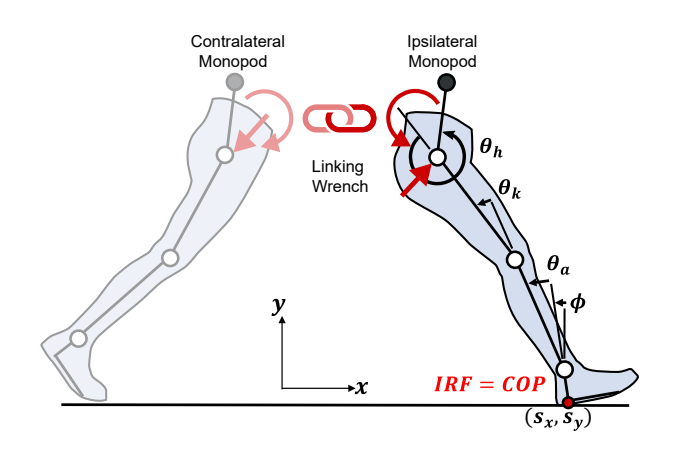


Fig. 2. Model of the human and exoskeleton lower-body system comprising linked monopods. COP denotes the center of pressure. IRF denotes inertial reference frame. Monopods are linked by equal and opposite wrench at torso. Controller is presented in the frame of the ipsilateral monopod.

A. Port-Controlled Hamiltonian Dynamics

We model each leg of the human-exoskeleton system as a 4-link sagittal plane monopod that starts from a floating foot and has three revolute joints (Fig. 2). This model is sufficient for our study where the actuator is assumed to be aligned with the joint in the sagittal plane. During the ipsilateral heel contact phase, the inertial reference frame is coincident with the position of the ipsilateral heel (s_x, s_y) . The global ipsilateral heel angle ϕ is defined with respect to the vertical axis. The ankle, knee, and hip angles of the ipsilateral leg are denoted θ_a , θ_k , and θ_h , respectively, while the contralateral side follows the same convention with the additional subscript 'C' (i.e., θ_{Ca} , θ_{Ck} , θ_{Ch}). The same convention is used to denote the contralateral heel position (s_{Cx}, s_{Cy}) and global foot angle ϕ_C . The model's masses and moments of inertia reflect the combination of the human and exoskeleton masses.

The dynamics of the ipsilateral and contralateral monopod models are linked by an interaction wrench at the hip center $F = [f_x, f_y, \tau_z]^T$ that acts equal and opposite on their respective torso bodies. The six degree-of-freedom ipsilateral monopod model has the generalized coordinates

$$q = [s_x, s_y, \phi, \theta_a, \theta_k, \theta_h]^T \in \mathbb{R}^6,$$

in the 6-dimensional configuration space \mathscr{Q} (Fig. 2). The conjugate momenta $p=M(q)\dot{q}\in\mathbb{R}^6$ are defined by the positive-definite inertia matrix $M(q)\in\mathbb{R}^{6\times 6}$ and the velocity vector \dot{q} . The port-controlled Hamiltonian dynamics can be characterized by the Hamiltonian $\mathcal{H}=\mathcal{H}(q,p):T^*\mathscr{Q}\to\mathbb{R}$, with $T^*\mathscr{Q}=\{(q,p)\mid q\in\mathscr{Q},\ p\in T_q^*\mathscr{Q}\}=\mathbb{R}^6\oplus\mathbb{R}^6$ (the cotangent bundle of \mathscr{Q}), through the equations

$$\begin{bmatrix} \dot{q} \\ \dot{p} \end{bmatrix} = \begin{bmatrix} 0_{6\times6} & I_{6\times6} \\ -I_{6\times6} & 0_{6\times6} \end{bmatrix} \nabla \mathcal{H} + \begin{bmatrix} 0_{6\times1} \\ \tau + A^T \lambda \end{bmatrix}, \tag{1}$$

where the skew-symmetric matrix above is known as the interconnection matrix. The Hamiltonian function $\mathcal{H}=\frac{1}{2}p^TM^{-1}(q)p+V(q)$ is given by the kinetic plus potential energy $V(q)\in\mathbb{R}$. The gradient $\nabla\mathcal{H}=[\partial_q\mathcal{H},\partial_p\mathcal{H}]^T$ is a column vector in \mathbb{R}^{12} with $\partial_q\mathcal{H},\partial_p\mathcal{H}\in\mathbb{R}^{1\times 6}$ as row vectors. Jacobian matrix $A\in\mathbb{R}^{c\times 6}$ maps the ground reaction force

Jacobian matrix $A \in \mathbb{R}^{c \times 6}$ maps the ground reaction force (GRF) vector $\lambda \in \mathbb{R}^c$ (acting at the heel) into equivalent joint torques in (1) (see [42]), where c is the number of constraints when the monopod is in stance. Given the holonomic contact constraints $a_\ell(q) = 0_{c \times 1}$ as shown in Fig. 3 (see [35]), the matrix A is derived via $A(q) = \partial_q a_\ell = [A_\ell(q), 0_{c \times 3}]$. Here, the subscript $\ell \in \{\text{heel}, \text{flat}, \text{toe}\}$ indicates the contact configuration. Noting that the time derivative of a_ℓ is given by $\dot{a}_\ell = A\dot{q} = A(\partial_p \mathcal{H})^T \equiv 0$, the Lagrange multiplier λ representing the GRF vector can be obtained by solving

$$\begin{split} \frac{d}{dt}[A(\partial_{p}\mathcal{H})^{T}] &= 0 \rightarrow \partial_{q}[A(\partial_{p}\mathcal{H})^{T}]\dot{q} + \partial_{p}[A(\partial_{p}\mathcal{H})^{T}]\dot{p} = 0 \\ \text{for } \lambda &= (A\partial_{p}^{2}\mathcal{H}A^{T})^{-1}\Big(-\partial_{q}[A(\partial_{p}\mathcal{H})^{T}](\partial_{p}\mathcal{H})^{T} \\ &+ A\partial_{p}^{2}\mathcal{H}[(\partial_{q}\mathcal{H})^{T} - \tau]\Big), \end{split}$$

where $\partial_p^2 \mathcal{H} = M^{-1} \in \mathbb{R}^{6 \times 6}$ denotes the second-order derivative of \mathcal{H} with respect to p. Note that functional dependencies are omitted to simplify notation here and throughout the paper.

The vector of joint torques $\tau \in \mathbb{R}^6$ aggregates the monopod's exoskeleton input $\tau_{\text{exo}} = Bu$ and human input $\tau_{\text{hum}} = Gv + J^T F$, with the Jacobian matrix J mapping the interaction wrench F into the monopod dynamics. The control inputs $u \in \mathbb{R}^m$ and $v \in \mathbb{R}^3$ respectively represent the exoskeleton and human torques (at the ankle, knee, and/or hip joints), which are mapped into the dynamics via matrices $B \in \mathbb{R}^{6 \times m}$ and $G \in \mathbb{R}^{6 \times 3}$, where m denotes the number of exoskeleton actuators with $1 \le m \le 3$. The system is underactuated with the number of generalized coordinates larger than the number of control inputs $(6 \ge m)$.

B. The Matching Conditions of the Monopod Controller

Assume we have closed the ipsilateral feedback loop for exoskeleton input u, while the human ipsilateral input v remains as an input to the Hamiltonian system. We consider a desired, closed-loop Hamiltonian $\tilde{\mathcal{H}}(p,q) = \frac{1}{2}p^T\tilde{M}^{-1}p + \tilde{V}$,

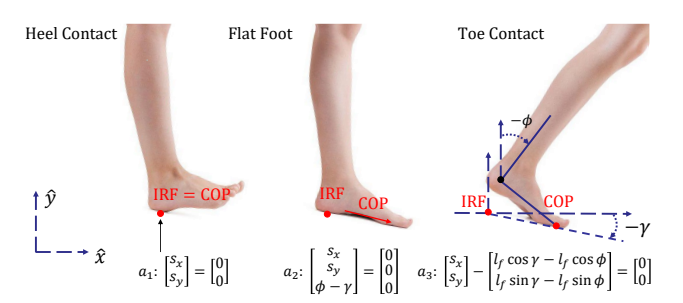


Fig. 3. Heel contact (left), flat foot (center), and toe contact (right) during the single-support period of human locomotion. Angle γ is the ground slope and l_f denotes the foot length. This figure is updated from [6].

where $\tilde{V} = V + \hat{V}$ represents the new potential energy with shaping term \hat{V} . The corresponding gravitational vector is $\tilde{N} = (\partial_q \tilde{V})^T = (\partial_q V)^T + (\partial_q \hat{V})^T = N + \hat{N} \in \mathbb{R}^6$. Similar to [33], we set $\tilde{M} = M$ to simplify the matching process and passivity proof and to avoid complicated calculations of the inertia matrix inverse in the control law. Hence, $\nabla \tilde{\mathcal{H}} = \nabla \mathcal{H} + [\partial_q \hat{V}, 0]^T$. Instead of modifying the inertia matrix, we achieve velocity-dependent shaping by modifying the interconnection matrix of the closed-loop Hamiltonian system.

The desired closed-loop dynamics based on $\tilde{\mathcal{H}}$ are

$$\begin{bmatrix} \dot{q} \\ \dot{p} \end{bmatrix} = \begin{bmatrix} 0 & I \\ -I & J_2 \end{bmatrix} \nabla \tilde{\mathcal{H}} + \begin{bmatrix} 0 \\ \tilde{\tau}_{\text{hum}} + A^T \tilde{\lambda} + B_x u_x \end{bmatrix}, \qquad (2)$$

where $B_x \in \mathbb{R}^{6 \times n_u}$ selects the n_u degrees of freedom that are measured but not actuated, and u_x represents the power leak resulting from their use in the control law (relaxing the matching conditions presented below). Together, these symbols refine the definition of the exogenous input $T_{\rm ex}$ from [33] to formalize its restriction to the image space of B_x . The human inputs v, F are mapped into the closed-loop dynamics by matrices \tilde{G} , \tilde{J} in $\tilde{\tau}_{\rm hum} = \tilde{G}v + \tilde{J}^T F$. The skew-symmetric matrix $J_2 = -J_2^T = (\partial_q Q)^T - \partial_q Q \in \mathbb{R}^{6 \times 6}$ represents the extra shaping degree-of-freedom from the interconnection structure of the IDA-PBC method [32], where $Q(q) \in \mathbb{R}^6$ is a smooth vector-valued function within the *artificial* gyroscopic terms $Q^T(\partial_p \mathcal{H})^T$. The closed-loop GRFs in (2) are represented by

$$\begin{split} \tilde{\lambda} &= (A\partial_{p^2}^2 \mathfrak{R} A^T)^{-1} \{ -\partial_q [A(\partial_p \mathfrak{R})^T] (\partial_p \mathfrak{R})^T \\ &+ A\partial_{p^2}^2 \mathfrak{R} [(\partial_q \tilde{\mathfrak{R}})^T - J_2 (\partial_p \mathfrak{R})^T - \tilde{G} v - \tilde{J}^T F - B_x u_x] \}. \end{split}$$

Based on standard results in [31], Hamiltonian systems (1) and (2) *match* if we have

$$\tau - \tilde{G}v - \tilde{J}^T F = Bu + \underline{Gv + J^T F - Gv - J^T F}$$

= $-(\partial_q \tilde{\mathcal{H}})^T + (\partial_q \mathcal{H})^T + J_2(\partial_p \mathcal{H})^T + A^T (\tilde{\lambda} - \lambda) + B_x u_x,$

where we choose the closed-loop mappings $\tilde{G} = G$ and $\tilde{J} = J$ such that the human inputs v and F disappear from the matching condition and control law as in [6]. By plugging in GRFs λ and $\tilde{\lambda}$ and following the steps in [32], we have

$$B_{\lambda}u = X_{\lambda}[-(\partial_q \tilde{\mathcal{H}})^T + (\partial_q \mathcal{H})^T + J_2(\partial_p \mathcal{H})^T + B_{\lambda}u_{\lambda}], \quad (3)$$

where $X_{\lambda} = I - A^T W A \partial_p^2 \mathcal{H} \in \mathbb{R}^{6 \times 6}$, $W = (A \partial_p^2 \mathcal{H} A^T)^{-1} \in \mathbb{R}^{c \times c}$, and $B_{\lambda} = X_{\lambda} B$. The corresponding *matching condition* is

$$0 = B_{\lambda}^{\perp} X_{\lambda} [-(\partial_{a} \tilde{\mathcal{H}})^{T} + (\partial_{a} \mathcal{H})^{T} + J_{2} (\partial_{p} \mathcal{H})^{T} + B_{x} u_{x}], \quad (4)$$

where $B_{\lambda}^{\perp} \in \mathbb{R}^{(6-m)\times 6}$ is any full-rank left annihilator of B_{λ} (satisfying $B_{\lambda}^{\perp}B_{\lambda}=0$). Note that the as-of-yet unspecified u_x relaxes this matching condition. For example, it allows for $\partial_q[\tilde{\mathcal{H}}-\mathcal{H}]$ to have non-zero values corresponding to the global angles measured by the IMUs. Because the global angles lack actuators to physically apply input u_x , the target energy shape is not perfectly achieved, i.e., there is a power leak from the target energy as discussed in Section II-D.

We can simplify the matching condition (4) by first decomposing matrix M into four sub-matrices as in [32]:

$$M = egin{bmatrix} M_1 & M_2 \ M_2^T & M_4 \end{bmatrix},$$

where $M_1 \in \mathbb{R}^{3\times 3}$ corresponds to the floating base joints (s_x, s_y, ϕ) and $M_4 \in \mathbb{R}^{3\times 3}$ corresponds to the joints $(\theta_a, \theta_k, \theta_h)$. Then we obtain

$$M^{-1} = \begin{bmatrix} \Delta^{-1} & -\Delta^{-1} M_2 M_4^{-1} \\ -M_4^{-1} M_2^T \Delta^{-1} & M_4^{-1} + M_4^{-1} M_2^T \Delta^{-1} M_2 M_4^{-1} \end{bmatrix},$$

where $\Delta = M_1 - M_2 M_4^{-1} M_2^T \in \mathbb{R}^{3 \times 3}$. As a result, we have $W = (A_\ell \Delta^{-1} A_\ell^T)^{-1}$ and X_λ can be expressed as

$$X_{\lambda} = \begin{bmatrix} I_{3\times3} - Z_{\lambda} & Z_{\lambda} M_2 M_4^{-1} \\ 0_{3\times3} & I_{3\times3} \end{bmatrix},$$

where $Z_{\lambda} = A_{\ell}^T W A_{\ell} \Delta^{-1} \in \mathbb{R}^{3 \times 3}$. Let $B = [0, b^T]^T$, where $b \in \mathbb{R}^{3 \times m}$ and rank(b) = m, and plug in X_{λ} to obtain $B_{\lambda} = [b^T M_4^{-1} M_2^T Z_{\lambda}^T, b^T]^T$. B_{λ} has the corresponding left annihilator

$$B_{\lambda}^{\perp} = egin{bmatrix} I_{3 imes 3} & -Z_{\lambda}M_2M_4^{-1} \ 0_{(3-m) imes 3} & b^{\perp} \end{bmatrix},$$

where $b^{\perp} \in \mathbb{R}^{(3-m)\times 3}$ is the (full-rank) left annihilator of b, i.e., $b^{\perp}b=0$. Plugging B_{λ}^{\perp} and X_{λ} into (4), we have

$$0 = \begin{bmatrix} I_{3\times3} - Z_{\lambda} & 0_{3\times3} \\ 0_{(3-m)\times3} & b^{\perp} \end{bmatrix} \cdot \begin{bmatrix} -(\partial_{q}\tilde{\mathcal{H}})^{T} + (\partial_{q}\mathcal{H})^{T} + J_{2}(\partial_{p}\mathcal{H})^{T} + B_{x}u_{x} \end{bmatrix} \\ = \begin{bmatrix} I_{3\times3} - Z_{\lambda} & 0_{3\times3} \\ 0_{(3-m)\times3} & b^{\perp} \end{bmatrix} [-\tilde{N} + N + J_{2}M^{-1}p + B_{x}u_{x}].$$
 (5)

The solution (5) of the matching condition gives the feasible structure of the closed-loop system.

Similarly, the six degree-of-freedom contralateral monopod has the generalized coordinates

$$q_{\mathrm{C}} = [s_{\mathrm{C}x}, s_{\mathrm{C}y}, \phi_{\mathrm{C}}, \theta_{\mathrm{C}a}, \theta_{\mathrm{C}k}, \theta_{\mathrm{C}h}]^T \in \mathbb{R}^6.$$

The port-controlled Hamiltonian dynamics can be characterized by the Hamiltonian $\mathcal{H}_{\rm C}=\mathcal{H}(q_{\rm C},p_{\rm C})=\frac{1}{2}p_{\rm C}^TM_{\rm C}^{-1}p_{\rm C}+V_{\rm C}$ with $N_{\rm C}=(\partial_{q_{\rm C}}V_{\rm C})^T$ through the equations

$$\begin{bmatrix} \dot{q}_{\rm C} \\ \dot{p}_{\rm C} \end{bmatrix} = \begin{bmatrix} 0_{6\times6} & I_{6\times6} \\ -I_{6\times6} & 0_{6\times6} \end{bmatrix} \nabla \mathcal{H}_{\rm C} + \begin{bmatrix} 0_{6\times1} \\ \tau_{\rm C} + A_{\rm C}^T \lambda_{\rm C} \end{bmatrix},$$

where $\tau_C \in \mathbb{R}^6$ aggregates the exoskeleton input $\tau_{Cexo} = B_C u_C$ with $u_C \in \mathbb{R}^{m_C}$ and the human input $\tau_{Chum} = G_C v_C - J_C^T F$ with the Jacobian matrix J_C . The constraint matrix is $A_C \in \mathbb{R}^{c_C \times 6}$. The desired closed-loop dynamics based on Hamiltonian $\tilde{\mathcal{H}}_C = \frac{1}{2} p_C^T M_C^{-1} p_C + \tilde{V}_C$, where $\tilde{V}_C = V_C + \hat{V}_C$, are given by

$$\begin{bmatrix} \dot{q}_{\rm C} \\ \dot{p}_{\rm C} \end{bmatrix} = \begin{bmatrix} 0 & I \\ -I & J_{\rm C2} \end{bmatrix} \nabla \tilde{\mathcal{H}}_{\rm C} + \begin{bmatrix} 0 \\ G_{\rm C} v_{\rm C} - J_{\rm C}^T F + A_{\rm C}^T \tilde{\lambda}_{\rm C} + B_{\rm Cx} u_{\rm Cx} \end{bmatrix},$$

with the exogenous input $B_{Cx}u_{Cx} \in \mathbb{R}^6$.

C. The Matching Conditions of the Bipedal Controller

Considering both monopod models together, we have a combined bipedal Hamiltonian $\mathcal{H}_{\rm B}=\mathcal{H}+\mathcal{H}_{\rm C}=\frac{1}{2}p_{\rm B}^TM_{\rm B}^{-1}p_{\rm B}+V_{\rm B},$ with combined vectors $q_{\rm B}=[q^T,q_{\rm C}^T]^T,\ p_{\rm B}=[p^T,p_{\rm C}^T]^T\in\mathbb{R}^{12}$ and $M_{\rm B}=\begin{bmatrix}M&0\\0&M_{\rm C}\end{bmatrix},\ N_{\rm B}=(\partial_{q_{\rm B}}V_{\rm B})^T=[\partial_{q_{\rm B}}(V+V_{\rm C})]^T=[N^T,N_{\rm C}^T]^T.$ The open-loop dynamics are given by

$$\begin{bmatrix} \dot{q}_{\mathrm{B}} \\ \dot{p}_{\mathrm{B}} \end{bmatrix} = \begin{bmatrix} 0_{12\times12} & I_{12\times12} \\ -I_{12\times12} & 0_{12\times12} \end{bmatrix} \nabla \mathfrak{H}_{\mathrm{B}} + \begin{bmatrix} 0_{12\times1} \\ \tau_{\mathrm{B}} + A_{\mathrm{B}}^T \lambda_{\mathrm{B}} \end{bmatrix},$$

where

$$\begin{array}{c}
\tau_{\mathrm{B}} \\
\hline
\begin{bmatrix} \tau \\ \tau_{\mathrm{C}} \end{bmatrix} =
\end{array}
\begin{array}{c}
B_{\mathrm{B}} \\
\hline
\begin{bmatrix} u \\ 0 \\ B_{\mathrm{C}} \end{bmatrix}
\end{array}
\begin{array}{c}
u_{\mathrm{B}} \\
u_{\mathrm{C}}
\end{array}
\begin{array}{c}
T_{\mathrm{HB}} \\
\hline
\begin{bmatrix} G_{\mathrm{B}} \\ 0 \\ 0 \\ G_{\mathrm{C}} \end{bmatrix}
\end{array}
\begin{array}{c}
v_{\mathrm{B}} \\
v_{\mathrm{C}}
\end{array}
\begin{array}{c}
J_{\mathrm{B}}^{T} \\
-J_{\mathrm{C}}^{T}
\end{array}
F,$$

subject to the kinematic constraint $J_B\dot{q}_B=0$. This constraint pertains to the velocity of the torso point, which can be defined in two ways: either with respect to the ipsilateral monopods, based on q, or the contralateral monopods, based on q_C . Under this constraint, the velocity of the torso point remains consistent. The GRFs are given by $\lambda_B = [\lambda^T, \lambda_C^T]^T \in \mathbb{R}^{c+c_C}$ with $A_B^T = \begin{bmatrix} A^T & 0 \\ 0 & A_C^T \end{bmatrix} \in \mathbb{R}^{12 \times (c+c_C)}$. The bipedal human torques, denoted by τ_{HB} , consist of both the ipsilateral and contralateral human joint inputs v_B and the interaction wrench F.

The closed-loop combined dynamics based on Hamiltonian $\tilde{\mathcal{H}}_{\rm B} = \tilde{\mathcal{H}} + \tilde{\mathcal{H}}_{\rm C} = \frac{1}{2} p_{\rm B}^T M_{\rm B}^{-1} p_{\rm B} + \tilde{V}_{\rm B}$ are given by

$$\begin{bmatrix} \dot{q}_{\rm B} \\ \dot{p}_{\rm B} \end{bmatrix} = \begin{bmatrix} 0 & I \\ -I & J_{\rm B2} \end{bmatrix} \nabla \tilde{\mathcal{H}}_{\rm B} + \begin{bmatrix} 0 \\ \tilde{\tau}_{\rm HB} + A_{\rm B}^T \tilde{\lambda}_{\rm B} + B_{{\rm B}x} u_{{\rm B}x} \end{bmatrix}, \quad (6)$$

where
$$\tilde{\lambda}_{B} = [\tilde{\lambda}^{T}, \tilde{\lambda}_{C}^{T}]^{T} \in \mathbb{R}^{c+c_{C}}$$
, $B_{Bx} = \begin{bmatrix} B_{x} & 0 \\ 0 & B_{Cx} \end{bmatrix}$, and $u_{Bx} = \begin{bmatrix} u^{T} & u^{T} \end{bmatrix}^{T}$. Similar to the monopod case, we choose the

 $\begin{bmatrix} u_x^T & u_{\mathrm{C}x}^T \end{bmatrix}^T$. Similar to the monopod case, we choose the closed-loop mapping matrices in $\tilde{\tau}_{\mathrm{HB}}$ such that the human inputs disappear from the matching condition and control law. The skew-symmetric interconnection structure is now $J_{\mathrm{B2}} = \begin{bmatrix} J_2 & 0 \\ 0 & J_{\mathrm{C2}} \end{bmatrix}$.

The open-loop and desired combined systems match if

$$B_{\mathbf{B}}u_{\mathbf{B}} = -(\partial_{q_{\mathbf{B}}}\tilde{\mathcal{H}}_{\mathbf{B}})^{T} + (\partial_{q_{\mathbf{B}}}\mathcal{H}_{\mathbf{B}})^{T} + J_{\mathbf{B}2}(\partial_{p_{\mathbf{B}}}\mathcal{H}_{\mathbf{B}})^{T} + A_{\mathbf{B}}^{T}(\tilde{\lambda}_{\mathbf{B}} - \lambda_{\mathbf{B}}) + B_{\mathbf{B}x}u_{\mathbf{B}x},$$

which does not depend on the human inputs τ_{HB} . Plugging GRFs into the matching condition above, we have

$$B_{B\lambda}u_{B} = X_{B\lambda}[-(\partial_{q_{B}}\tilde{\mathcal{H}}_{B})^{T} + (\partial_{q_{B}}\mathcal{H}_{B})^{T} + J_{B2}(\partial_{p_{B}}\mathcal{H}_{B})^{T} + B_{Bx}u_{Bx}],$$
(7)

where

$$X_{\mathrm{B}\lambda} = \begin{bmatrix} X_{\lambda} & & & & & \\ I - A^{T}WA\partial_{p}^{2}\mathcal{H} & & & & & \\ & & & & X_{\mathrm{C}\lambda} & & \\ & 0 & & I - A_{\mathrm{C}}^{T}W_{\mathrm{C}}A_{\mathrm{C}}\partial_{p_{\mathrm{C}}}^{2}\mathcal{H}_{\mathrm{C}} \end{bmatrix} \in \mathbb{R}^{12 \times 12}$$

$$B_{\mathrm{B}\lambda} = X_{\mathrm{B}\lambda}B_{\mathrm{B}} = \begin{bmatrix} X_{\lambda}B & & & & \\ & 0 & & X_{\mathrm{C}\lambda}B_{\mathrm{C}} \end{bmatrix} \in \mathbb{R}^{12 \times (m+m_{\mathrm{C}})}.$$

The matching condition corresponding to (7) becomes

$$0 = B_{\mathrm{B}\lambda}^{\perp} X_{\mathrm{B}\lambda} [-(\partial_{q_{\mathrm{B}}} \tilde{\mathcal{H}}_{\mathrm{B}})^{T} + (\partial_{q_{\mathrm{B}}} \mathcal{H}_{\mathrm{B}})^{T} + J_{\mathrm{B}2} (\partial_{p} \mathcal{H}_{\mathrm{B}})^{T} + B_{\mathrm{B}x} u_{\mathrm{B}x}],$$
(8)

5

where $B_{\mathrm{B}\lambda}^{\perp} \in \mathbb{R}^{(12-m-m_{\mathrm{C}})\times 12}$ is the (full-rank) left annihilator of $B_{\mathrm{B}\lambda}$, i.e., $B_{\mathrm{B}\lambda}^{\perp}B_{\mathrm{B}\lambda}=0$. Following the previous matrix decomposition and simplification, we have

$$B_{\mathrm{B}\lambda}^{\perp} = egin{bmatrix} I_{3 imes 3} & -Z_{\lambda}M_{2}M_{4}^{-1} & 0 & 0 \ 0_{(3-m) imes 3} & b^{\perp} & 0 & 0 \ 0 & 0 & I_{3 imes 3} & -Z_{\mathrm{C}\lambda}M_{\mathrm{C}2}M_{\mathrm{C}4}^{-1} \ 0 & 0 & 0_{(3-m_{\mathrm{C}}) imes 3} & b^{\perp}_{\mathrm{C}} \end{bmatrix}$$

Plugging $B_{\mathrm{R}\lambda}^{\perp}$, $X_{\mathrm{B}\lambda}$ into (8), the matching condition becomes

$$0 = \begin{bmatrix} I_{3\times3} - Z_{\lambda} & 0 & 0 & 0\\ 0_{(3-m)\times3} & b^{\perp} & 0 & 0\\ 0 & 0 & I_{3\times3} - Z_{C\lambda} & 0\\ 0 & 0 & 0_{(3-m_{C})\times3} & b_{C}^{\perp} \end{bmatrix} \cdot (9)$$
$$\left[-(\partial_{q_{B}} \tilde{\mathcal{H}}_{B})^{T} + (\partial_{q_{B}} \mathcal{H}_{B})^{T} + J_{B2}(\partial_{p_{B}} \mathcal{H}_{B})^{T} + B_{Bx} u_{Bx} \right],$$

which shows the feasible modular structure of the closed-loop system using underactuated energy shaping control, i.e., $\mathscr{U} := [\partial_{q_B}(\mathcal{H}_B - \tilde{\mathcal{H}}_B)]^T + J_{B2}(\partial_{p_B}\mathcal{H}_B)^T + B_{Bx}u_{Bx}$ must be in the null space of $B_{B\lambda}^{\perp}X_{B\lambda}$. We find a solution to (9) by recognizing that we can only shape \mathscr{U} to be in the range space of B_B .

Rewriting (7) and plugging in the solution of (9), we have

$$0 = X_{\mathrm{B}\lambda}(B_{\mathrm{B}}u_{\mathrm{B}} - \mathscr{U}).$$

By making $B_B u_B = \mathcal{U}$, the above equation is satisfied. A solution exists for $B_B u_B = \mathcal{U}$ since $B_B B_B^+ \mathcal{U} = \mathcal{U}$ [43], where $B_B^+ = (B_B^T B_B)^{-1} B_B^T$. The solution is unique since B_B has full column rank. From this, we obtain the simplified control law that is independent of the GRFs:

$$u_{\rm B} = B_{\rm B}^+ \mathcal{U} = B_{\rm B}^+ [N_{\rm B} - \tilde{N}_{\rm B} + J_{\rm B2} M_{\rm B}^{-1} p_{\rm B} + B_{\rm Bx} u_{\rm Bx}],$$
 (10) with the assumption that

$$B_{\mathrm{B}} = \begin{bmatrix} 0 & b^T & 0 & 0 \\ 0 & 0 & 0 & b_{\mathrm{C}}^T \end{bmatrix}^T$$

and the corresponding left pseudoinverse

$$B_{\rm B}^+ = \begin{bmatrix} b^T b & 0 \\ 0 & b_{\rm C}^T b_{\rm C} \end{bmatrix}^{-1} \begin{bmatrix} 0 & b^T & 0 & 0 \\ 0 & 0 & 0 & b_{\rm C}^T \end{bmatrix}.$$

Although the null space of $B_{\rm B}^+ \in \mathbb{R}^{(m+m_{\rm C})\times 12}$ is not empty, $u_{\rm B}$ is generally non-zero due to $\mathscr{U} \in {\rm range}(B_{\rm B})$ designed according to (9) and the full column rank matrices $b, b_{\rm C}$.

Note that the energy shaping framework can be applied to the bipedal model with an arbitrary configuration of assisted joints. Considering the simple example of bilateral knee exoskeletons $(m=m_{\rm C}=1, \text{ a symmetric single-joint configuration})$, we have $b=b_{\rm C}=\begin{bmatrix}0&1&0\end{bmatrix}^T$ and $b^\perp=b_{\rm C}^\perp=\begin{bmatrix}1&0&0\\0&0&1\end{bmatrix}$. By zeroing the unactuated rows of $N_{\rm B}-\tilde{N}_{\rm B}+J_{\rm B2}M_{\rm B}^{-1}p_{\rm B}+J_{\rm B2}u_{\rm B2}$ from (10), i.e., those associated with $(s_x,s_y,\phi,\theta_a,\theta_h,s_{\rm Cx},s_{\rm Cy},\phi_{\rm C},\theta_{\rm Ca},\theta_{\rm Ch})$, this expression is in the range space of $B_{\rm B}$ and thus in the null space of $B_{\rm B\lambda}^\perp X_{\rm B\lambda}$, satisfying the matching condition (9) with the flexibility to design the skew-symmetric matrix $J_{\rm B2}$ and $\tilde{N}_{\rm B}$.

D. Control Law with Relaxed Passivity and Stability

Our control objective is to offer partial torque assistance while allowing the human to control their kinematics across activities. Ultimately, it is the human's responsibility to maintain stability, whether through joint impedance control [44] or other means. Our control method leverages the passivity property to ensure that stabilization does not become more difficult due to exoskeleton interaction. Energetic passivity is formally defined in [45] as follows.

Definition II.1. Consider a general mechanical system

$$\dot{x} = f(x, u), \quad y = h(x, u),$$
 (11)

where $x \in \mathbb{R}^n$, $u \in \mathbb{R}^p$ is the input and $y \in \mathbb{R}^p$ is the output. Let $E(x) : \mathbb{R}^n \to \mathbb{R}$ be a continuously differentiable, positive semi-definite function, then the system (11) is passive from input u to output y if $\dot{E}(x) = \frac{\partial E}{\partial x} f(x, u) \leq y^T u$.

By strict use of energy shaping control, the target Hamiltonian will satisfy $\dot{\mathcal{H}}_{\rm B} \leq \dot{q}_{\rm B}^T \tau_{\rm HB}$, or, in other words, serve as a passivity certificate for the closed loop system with respect to the remaining human input (ensuring the human controls energy injection). However, for various practical reasons, we introduce relaxations to this property, which we describe together through a "power leak,"

human input power leaks
$$\dot{\tilde{\mathcal{H}}}_{B} \leq \overbrace{\dot{q}_{B}^{T} \tau_{HB}}^{human input} + \overbrace{\dot{q}_{B}^{T} \tilde{T}_{Bex}}^{power leaks}, \qquad (12)$$

where \tilde{T}_{Bex} represents the 'leak' torque vector. The three contributions to this leak are 1) use of global angle information without associated actuators (i.e., relaxing matching conditions using the exogenous input $B_{\text{Bx}}u_{\text{Bx}}$), 2) use of vertical ground reaction force to scale torques, and 3) nonlinear negative power tapering which lets the human, rather than the exoskeleton, store mechanical energy in behaviors like initiating a squat.

The first modification replicates the trick introduced in [33]. Normally, the use of the global information from IMUs to define a change in the Hamiltonian results in q-partial derivatives, or torques, that cannot be produced by the underactuated input. This means the target behavior cannot be achieved by the underactuated input. However, by introducing an exogenous input that directly cancels these unachievable torques, we can instead say that the target system has been achieved with a power leak due to the fictitious exogenous input. Since the target system is not perfectly achieved, the underactuated control law can generate non-zero net work where the power leak accounts for the opposite of the non-zero net work. The exogenous input which achieves this cancellation was first introduced as $T_{\rm ex}$ in [33], with the restriction to the image space of $B_{\rm Bx}$ implied but not formally stated.

Vertical ground reaction force (vGRF) scaling prevents excessive torque as weight transfers from the assisted leg to the contralateral leg during double support [46]. This scaling $\mathcal{G}(vGRF, \xi)$ is defined via the sigmoid functions, where

$$\begin{split} \mathscr{G}(\textit{vGRF}, \xi) &= \sum_{i}^{\textit{w}} \alpha_{i} \big[\kappa_{i1} g_{\text{st}} \big(\textit{vGRF} \big) + \kappa_{i2} g_{\text{sw}} \big(\textit{vGRF} \big) + \kappa_{i3} \big] \xi_{i}, \\ g_{\text{st}} &:= \frac{\textit{vGRF}}{1 + e^{-a \cdot (\textit{vGRF} - b)}}, \quad g_{\text{sw}} &:= \frac{e^{-a \cdot (\textit{vGRF} - b)}}{1 + e^{-a \cdot (\textit{vGRF} - b)}}, \end{split}$$

with scalar constants $\kappa_{i1,i2,i3}$ and the linear combination $\xi = \sum_{i}^{w} \alpha_{i} \xi_{i}$ of w vectors $\xi_{i} \in \mathbb{R}^{12}$. The incorporation of vGRF scaling is an essential aspect of our proposed control scheme. Depending on the defined basis in Section II-E, the vGRF scaling can take the form of either $g_{st}(vGRF)$ or $g_{sw}(vGRF)$, and is utilized to ensure a smooth transition between the stance and swing phases. This approach also enables us to employ a single controller for both the stance and swing phases, replacing the hybrid control scheme presented in [33].

The negative power tapering strategy is included for the comfort of the subjects. The controller can perform negative work (which can then be released as positive work), and such behavior is key to energetic passivity. However, based on the feedback from some subjects during pilot testing, negative work assistance was undesirable during certain phases of stair descent, ramp descent, and stand-to-sit transitions. Therefore, we apply a negative power tapering strategy, where control torques τ producing negative power are scaled down by the pointwise operator $\mathscr{F}: \mathbb{R}^m \to \mathbb{R}^m$ defined by

$$\mathscr{F}_{i}(\tau) = \begin{cases} e^{-\beta \|\tau_{i} \cdot \dot{\theta}_{i}\|} \cdot \tau_{i}, & \text{if } \tau_{i} \dot{\theta}_{i} < 0 \\ \tau_{i}, & \text{otherwise} \end{cases}$$
 (13)

where τ_i is the i^{th} joint control torque, $\dot{\theta}_i$ is the i^{th} joint velocity and β is the tapering coefficient.

Altogether, the control law (10) satisfying (7)-(9) becomes

$$u_{\rm B} = B_{\rm B}^{+}(-\hat{N}_{\rm B} + J_{\rm B2}M_{\rm B}^{-1}p_{\rm B} + \tilde{T}_{\rm Bex})$$

$$= B_{\rm B}^{+}\mathscr{F}\Big(\mathscr{G}(vGRF, -\hat{N}_{\rm B} + J_{\rm B2}M_{\rm B}^{-1}p_{\rm B} + B_{\rm Bx}u_{\rm Bx})\Big).$$
(14)

This control law is independent of the human inputs and dependent on velocity via the conjugate momenta $p_{\rm R}$.

To extend our previous port-Hamiltonian control paradigm in [33, Eq. (2)], we redefine the exogenous input as

$$\tilde{T}_{\text{Bex}} = \mathscr{F} \Big(\mathscr{G}(vGRF, -\hat{N}_{\text{B}} + J_{\text{B2}}M_{\text{B}}^{-1}p_{\text{B}} + B_{\text{Bx}}u_{\text{Bx}}) \Big)$$
$$+ (\hat{N}_{\text{B}} - J_{\text{B2}}M_{\text{B}}^{-1}p_{\text{B}}),$$

which now includes the composite "power leak" associated with the combination of unactuated global variables, vGRF scaling, and negative power tapering. As a result, we can still satisfy matching condition (9) and use the target dynamic equation to describe the system while incorporating the (unactuated) global variables ϕ and ϕ_C into the actuated part of \hat{N}_B and $J_{B2}M_B^{-1}p_B$. Given the similar structure of (6) as in [33], relaxed input-output passivity is summarized as follows.

Proposition II.1. If the new potential energy shaping term \hat{V}_B is continuously differentiable, then the closed-loop system (6) is passive with two input ports: the human input with effort τ_{HB} and flow \dot{q}_B , and the power leak port with effort \tilde{T}_{Bex} and flow \dot{q}_B .

Proof. The detailed proof is in [33], Proposition 3.1.
$$\Box$$

Moreover, if the human is assumed to modulate joint impedance [6], [44] and provide the exogenous input \tilde{T}_{Bex} , stability can be shown in the sense of Lyapunov.

Proposition II.2. Consider the closed-loop system (6) with equilibrium point $(q_B^*, 0)$ where the forces along the shaped

potential energy balance the muscular forces and the GRFs, i.e., $N_{\rm B}+\hat{N}_{\rm B}-\tau_{\rm HB}-A_{\rm B}^T\tilde{\lambda}_{\rm B}(q_{\rm B}^\star,0)-\tilde{T}_{\rm Bex}=0$. This equilibrium point is stable in the sense of Lyapunov given human input $\tau_{\rm HB}=-K_pe-K_d\dot{e}-\tilde{T}_{\rm Bex}$, where the constant diagonal matrices K_p , K_d are positive semi-definite, and $e=q_{\rm B}-\bar{q}_{\rm B}$ represents the difference between $q_{\rm B}$ and the human's constant set-point vector $\bar{q}_{\rm B}$.

Proof. The detailed proof is in [33], Proposition 3.2. \Box

E. Constructing a Modular Basis for the Controller

To guarantee satisfaction of our matching conditions, we simply parameterize our controller (our target energy and target interconnection matrix) using a functional basis where each element satisfies the conditions. This section demonstrates how such a basis can be built using simple primitives. For example, we use the sine-cosine primitive, $\mathcal{B}_{sc}(x) = (\sin(x), \cos(x))$, to express behavior resembling the gravitational potential energy of a pendulum. But to more fully express the potential for a single joint to modify potential energy, we expand this. The following single degree of freedom Hamiltonian modification primitive describes potential energy alterations that only affect one active joint, q_x , with one unactuated angle reference ϕ_x (i.e., a global angle measured by an IMU) available:

$$\begin{split} \Delta\mathcal{H}_{1\text{grav}}(q_x,\phi_x) &= \left(q_x,\ \frac{1}{2}q_x^2,\ \mathcal{B}_{\text{sc}}(q_x),\ \frac{1}{2}\mathcal{B}_{\text{sc}}(2q_x)\right. \\ &\left.q_x\mathcal{B}_{\text{sc}}(\phi_x),\ \mathcal{B}_{\text{sc}}(\phi_x+q_x),\ \frac{1}{2}\mathcal{B}_{\text{sc}}(\phi_x+2q_x)\right)\alpha_{1\text{grav}}. \end{split}$$

In our notation, to use this basis for the ipsilateral knee we would substitute $q_x = \theta_k$ and $\phi_x = \phi + \theta_a$. Choosing the target Hamiltonian as $\tilde{\mathcal{H}} = \mathcal{H} + \Delta \mathcal{H}_{1\text{grav}}$ would then result in an active joint torque and a power leak equal to $\dot{\phi}_x \partial_{\phi_x} \Delta \mathcal{H}_{1\text{grav}}$.

Adding a second active joint introduces the potential for not only two copies of the first basis, but also additional coupling potential energy terms. For example, with one unactuated angle reference ϕ_x we can define the basis

$$\begin{split} &\mathcal{B}_{\mathcal{H}h2}(q_a, q_b, \phi_x) = \\ &\left(\mathcal{B}_{sc}(\phi_x + q_a + q_b), \ \frac{1}{2}\mathcal{B}_{sc}(\phi_x + 2q_a + 2q_b), \\ &\mathcal{B}_{sc}(\phi_x + 2q_a + q_b), \ \mathcal{B}_{sc}(\phi_x + q_a + 2q_b)\right), \end{split}$$

and with two unactuated angle references,

$$\begin{split} \Delta \mathcal{H}_{2\mathrm{grav}}(q_a, q_b, \phi_a, \phi_b) &= \Big(\mathscr{B}_{\mathcal{H}\mathrm{h2}}(q_a, q_b, 0), \\ \mathscr{B}_{\mathcal{H}\mathrm{h2}}(q_a, q_b, \phi_a), \ \mathscr{B}_{\mathcal{H}\mathrm{h2}}(q_a, q_b, \phi_b) \Big) \alpha_{2\mathrm{grav}}. \end{split}$$

This second unactuated angle reference is typically an IMU on the other leg.

Multiple joints also introduce the possibility of a non-trivial interconnection matrix, J_2 . We have great freedom in parameterizing the upper triangular elements of this (skew-symmetric) matrix. Unlike the modifications to potential energy, the basis for J_2 does not need a power leak through $B_x u_x$ to make use of unactuated measurements (like global link angles). Any skew-symmetric matrix will similarly conserve energy. However,

for simplicity, we parameterize $J_2(q)$ to depend on the same measurements as the two-joint Hamiltonian basis above,

$$\begin{split} J_2(q) &= \begin{bmatrix} 0 & j(q) \\ -j(q) & 0 \end{bmatrix}, \text{ where } j(q_a, q_b, \phi_a, \phi_b) = \\ & \left(1, \mathcal{B}_{h1}(q_a, \phi_a), \ \mathcal{B}_{h1}(q_b, \phi_b), \ \mathcal{B}_{h2}(q_a, q_b, 0), \right. \\ & \left. \mathcal{B}_{h2}(q_a, q_b, \phi_a), \ \mathcal{B}_{h2}(q_a, q_b, \phi_b) \right) \alpha_{2 \text{gyro}}. \end{split}$$

Here, the single degree of freedom helper basis is

$$\mathcal{B}_{h1}(q_a, \phi_x) = \Big(q_a, \ \mathcal{B}_{sc}(q_a), \ \mathcal{B}_{sc}(2q_a), \ \mathcal{B}_{sc}(\phi_x),$$

 $\mathcal{B}_{sc}(q_a + \phi_x), \ \mathcal{B}_{sc}(2q_a + \phi_x)\Big),$

the helper basis for combinations of two joints (and one inertial reference) is

$$\begin{split} \mathscr{B}_{\text{h2}}(q_a,q_b,\phi_x) &= \Big(\mathscr{B}_{\text{sc}}(\phi_x + q_a + q_b), \ \mathscr{B}_{\text{sc}}(\phi_x + 2q_a + 2q_b), \\ \mathscr{B}_{\text{sc}}(\phi_x + 2q_a + q_b), \ \mathscr{B}_{\text{sc}}(\phi_x + q_a + 2q_b) \Big). \end{split}$$

These primitives are then combined to create bases for the control law. For example, the law we apply for a bilateral single-joint exoskeleton configuration with measurements q_x , \dot{q}_x , ϕ_x , and $vGRF_x$ denoting actuated angle, actuated joint angular rate, unactuated angle (global angle reference), and vertical component of the ground reaction force for each side $x \in a, b$, we define the basis for the control torque as

$$\mathcal{B}_{u}(q_{a}, q_{b}, \phi_{a}, \phi_{b}, vGRF_{a}, vGRF_{b}, \dot{q}_{a}, \dot{q}_{b}) = \begin{pmatrix} D_{1} & D_{2} & 0 & 0 & C_{1} & C_{2} \\ 0 & 0 & D_{3} & D_{4} & C_{3} & C_{4} \end{pmatrix},$$

$$(15)$$

where the decoupled terms are

$$\begin{split} D_1 &= \mathsf{g}_{\mathrm{st}}(vGRF_a)\partial_{q_a}\Delta\mathcal{H}_{1\mathrm{grav}}(q_a,\phi_a), \\ D_2 &= \mathsf{g}_{\mathrm{sw}}(vGRF_a)\partial_{q_a}\Delta\mathcal{H}_{1\mathrm{grav}}(q_a,\phi_a), \\ D_3 &= \mathsf{g}_{\mathrm{st}}(vGRF_b)\partial_{q_b}\Delta\mathcal{H}_{1\mathrm{grav}}(q_b,\phi_b), \\ D_4 &= \mathsf{g}_{\mathrm{sw}}(vGRF_b)\partial_{q_b}\Delta\mathcal{H}_{1\mathrm{grav}}(q_b,\phi_b), \end{split}$$

and the coupled terms are

$$\begin{split} C_1 &= \partial_{q_a} \Delta \mathcal{H}_{2\text{grav}}(q_a, q_b, \phi_a, \phi_b), \quad C_2 = j(q_a, q_b, \phi_a, \phi_b) \dot{q}_b, \\ C_3 &= \partial_{q_b} \Delta \mathcal{H}_{2\text{grav}}(q_a, q_b, \phi_a, \phi_b), \quad C_4 = -j(q_a, q_b, \phi_a, \phi_b) \dot{q}_a. \end{split}$$

For the single-joint unilateral case, only D_1 and D_2 would be needed to construct the basis. While the inclusion of global angle references into the design complicates the expression of a simple pattern for scaling this basis to larger configurations of joints, the essential technique is to include terms like D_1 and D_2 for each joint, and to leave the interconnection terms free of the influence of the vGRF. The restriction of the basis to those degrees of freedom which are either actuated (q_x terms) or measured but unactuated (ϕ_x terms) is enough to guarantee the satisfaction of our relaxed matching conditions. The selection of basis functions in our paper is based on a grid search. We determine the number of basis functions in Section II-F by applying "L1 regularization."

F. Design Optimization

In [33], we formed multiple basis functions for the shaping terms in (3) and optimized their coefficients to fit weight-normalized able-bodied joint torque data (given able-bodied input data) over a broad set of activities. The parameters were obtained by running "fmincon" with sequential quadratic programming in MATLAB. In this paper, we re-design the optimization problem to fit with "CVX [47]", which calculates the parameters more efficiently and enforces disciplined convex programming rules [48].

Similar to [33], we design $-\hat{N}_B + J_{B2}M_B^{-1}p_B + B_{Bx}u_{Bx}$ as a linear combination of the basis functions $\{\xi_1, \xi_2, ..., \xi_w\}$ with the constant coefficients $\alpha \in \mathbb{R}^w$ and vGRF scaling \mathscr{G} , where w basis functions $\xi_i \in \mathbb{R}^{12}$ follow the structure of (9). The control law (14) is thus given as

$$u_{B} = B_{B}^{+} \mathscr{F} \Big(\mathscr{G}(vGRF, \alpha_{1}\xi_{1} + \dots + \alpha_{w}\xi_{w}) \Big)$$
$$= \mathscr{F} \Big(\mathscr{B}_{u}(q, p, vGRF) \kappa \Big),$$

where $\mathscr{B}_u(q, p, \nu GRF) \in \mathbb{R}^{(m+m_C) \times \bar{w}}, \ \kappa \in \mathbb{R}^{\bar{w}}.$

As mentioned in [9], an assistive torque profile proportional to the average biological torque may not be the optimal assistance torque for human subjects. Moreover, based on feedback from the subjects during pilot testing, biomimetic knee extension during late stance resists the subjects lifting their legs. Instead of fitting the target joint torques to normalized ablebodied joint torques as in [33], we optimize the constant coefficients κ so the outputs of control law $U = \mathcal{B}_u(q, p, \nu GRF)\kappa$ best fit a weighted combination $Y = \Gamma_1 Y_h + \Gamma_2 Y_g + \Gamma_3 Y_0$ of the normalized able-bodied joint torques Y_h , gravity-shaping joint torques Y_g , and zero (passive) joint torques Y_0 , where $\Gamma_1 + \Gamma_2 + \Gamma_3 = I$ are diagonal weighting matrices for different phases. The optimization problem is defined as

$$\min_{\kappa, t_1, t_2, \mathbf{S}_j} t_1 + \Lambda_1 t_2 + \Lambda_2 \sum_j \mathbf{1}^T \mathbf{S}_j$$
 (16)

subject to

$$\sum_{j} ||U_{j}(q_{j}, p_{j}, \kappa, \nu GRF) - Y_{j})||_{2}^{W_{j}} \leq t_{1}, \quad ||\kappa||_{1}^{W_{s}} \leq t_{2},$$

$$-Y_{j} \odot U_{j}(q_{j}, p_{j}, \kappa, \nu GRF) \leq \mathbf{S}_{j}, \quad \mathbf{S}_{j} \geq 0, \quad \forall j,$$

where the subscript j represents the number of different locomotor tasks, including level-ground walking, ramp walking, stair climbing, and stand-to-sit. The state vectors $q_j, p_j \in \mathbb{R}^{n \times 9}$ comprise samples over time (n total) for the given task j. The two-norm of a vector with weighting matrix W is denoted as $\|\cdot\|_2^W$. Hyperparameters employed in the optimization problem are established through a grid search process.

The objective function comprises three parts, where scalar t_1 corresponds to the least squares error of the exoskeleton control inputs $U_j \in \mathbb{R}^{(m+m_C)n}$ and the target joint torques $Y_j \in \mathbb{R}^{(m+m_C)n}$, with the weighting diagonal matrix W_j of different tasks. Scalar t_2 represents "L1 regularization" to enforce sparsity in the model by zeroing the least important parameters in vector κ , which avoids over-fitting and improves the prediction of untrained tasks as in [33]. The third part $\mathbf{1}^T \mathbf{S}_j$ (different from [33]) corresponds to the cost of opposite signs between the exoskeleton control torques and the target torques

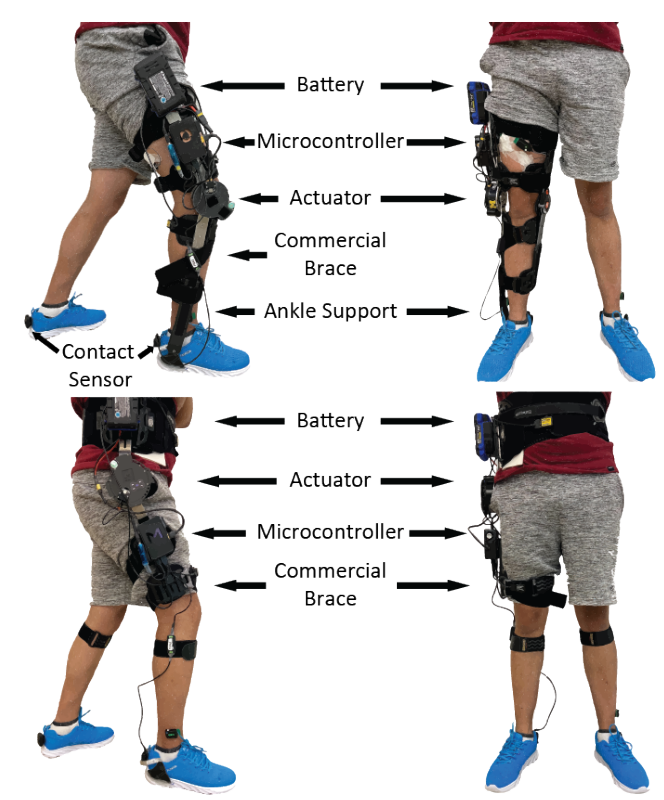


Fig. 4. *M-BLUE* hip-only and knee-only exoskeleton configurations worn by a healthy user (with an unpowered ankle brace in the knee-only configuration to support the mass of the knee actuator).

to emphasize the importance of assisting rather than resisting human torques. Vector $\mathbf{S}_j \in \mathbb{R}^n$ represents the slack for the sign difference, and $c = a \odot b$ denotes the pointwise product with $c_i = a_i b_i$. The terms Λ_i weight the different costs.

We use "CVX [47]" in MATLAB to find the optimal solution κ^* . Leveraging kinematic and kinetic data from nine subjects across different walking conditions [49] and stand-to-sit transitions [50] allows our controller to adapt more effectively and minimize sensitivity to variations in the movements of different users. The vGRFs during locomotion tasks in [49], [50] are normalized by body weight. The training gaits include level treadmill walking at 0.5, 1.5m/s, ascending/descending ramps with inclines of 5.2°, 11°, and ascending/descending stairs with step height of 4, 7 inch [49]. The corresponding controller provides assistance torques $\tau_{\rm exo} = \mathcal{F}(\mathcal{B}_u(q,p,vGRF)\kappa^*)$. Weight LOA%, where LOA% (level-of-assistance) scales down the controller to a desired fraction of normative torque. The optimal parameters κ^* are ultimately used in the real-time implementation presented next.

III. EXPERIMENTAL METHODS

In this section, we implement the *M-TOES* controller on the *M-BLUE* exoskeleton system, and present the experimental methods for validating different configurations with healthy human subjects performing multiple activities of daily life.

A. Hardware Implementation

The controller was implemented on bilateral and unilateral knee or hip configurations of *M-BLUE* in Fig. 4 (see [10] for details). Each knee and hip module weighs 2.36 kg and

2.15 kg, respectively, including the battery (470 g). *M-BLUE* combines commercial off-the-shelf orthoses with a quasi-direct drive actuator—the T-motor AK80-9 which comprises a high-torque electric motor with an internal 9:1 plenary gearbox. This actuator is highly backdrivable with less than 0.5 Nm static backdrive torque. It can provide 9 Nm continuous torque and 18 Nm peak torque according to the manufacturer, though our bench-top calibration in [10] verified up to 30 Nm peak torque using the Dephy FASTER ActPack driver.

M-BLUE was powered by a 24 V, 2 Amp-hour Kobalt powertool battery (~470 g) attached to a 3D printed adapter mounted on the side of each orthosis. The high-level control loop ran at ~ 200 Hz on a Raspberry Pi 4B for each leg, where bilateral configurations communicated through ZeroMQ, a TCP-based package. Sagittal-plane joint angles and global segment angles were measured by two 6-axis IMUs (3DM-GX5-25, LORD Microstrain) attached to the brace straps around each limb segment. Soft-tissue and strap compliance caused vibrations when using the actuator encoders in the feedback loop, due to differences between the measured exoskeleton joint angle and the actual human joint angle. To address this issue, we utilized IMU-based joint measurements (difference between the global angles of adjacent segments), with IMUs positioned on the frontal thigh and shank to minimize the impact of assistive torque in the sagittal plane.

The vGRF was measured by a commercial footwear sensor (IEE Smart Footwear) placed underneath the shoe insole. Similar to zero-order hold, a parallel thread was created to read vGRF continuously at ~ 55 Hz, which avoided slowing down the main control loop at 200 Hz. The sensor was calibrated using a predefined calibration procedure before each use to achieve a final readout normalized to body weight in the same manner as the vGRFs from the dataset used for the controller simulation. An infinite impulse response second-order low-pass filter (50 Hz cutoff frequency) was applied to the vGRF to reduce noise. The negative power tapering coefficient β in (13) was adjusted for user comfort during several practice trials and fixed for all subjects during data collection.

Safety features included hard stops, thermal protectors, software interventions, and current limiters. We also implemented a motor current limiting policy to prevent overheating the motor windings as described in the Appendix.

B. Human Subject Methods

The study was approved by the Institutional Review Board at the University of Michigan (HUM00201957). We enrolled eight able-bodied (AB) human subjects (see Table I) to demonstrate the ability of *M-BLUE* with *M-TOES* to assist multiple tasks. We assessed muscle activation via wireless EMG (Delsys Inc.) of vastus medialis oblique (VMO), rectus femoris (RF), biceps femoris (BF), gluteus maximus (GLUT), which function as a knee extensor, knee extensor/hip flexor, knee flexor, hip extensor, respectively. We used neonatal sensors for VMO, RF, and BF.

Participants performed the same activities of daily life with five exoskeleton conditions: bare (no exoskeleton), active bilateral hip exoskeleton (HipB), active unilateral hip exoskeleton

TABLE I SUBJECT DEMOGRAPHICS

Subject	AB01	AB02	AB03	AB04	AB05	AB06	AB07	AB08
Sex	M	M	F	M	F	M	F	F
Mass (kg)	80	80	60	88	63	70	55	58



Fig. 5. AB01 with bilateral knee *M-BLUE* walked on a circuit. One trial consists of Part 1 (P1) and Part 2 (P2).

(HipU), active bilateral knee exoskeleton (KneeB), and active unilateral knee exoskeleton (KneeU). The LOA% for the active modes was set based on the subjects' comfort level during practice trials and fixed for the entire experiment. Each trial comprised two parts of an activity circuit at a self-selected speed, as shown in Fig. 5. Part 1 (P1) includes five sections: stand-sit cycle (SS), followed by incline walking (II, 12°), level walking on the platform, stair descent (SD, 6 inch), and level walking (LL) over ground. Part 2 (P2) reverses the direction: stand-sit cycle, followed by level walking over ground, stair ascent (SA, 6 inch), level walking on the platform, and decline walking (DD, 12°). All incline/decline and upstairs/downstairs sections started with the right foot contacting the ramp/stairs first to get the maximum number of strides for the right leg (not required for level walking). We collected 5 trial repetitions for each exoskeleton condition, providing a minimum of 20 gait cycles of level walking, 10 gait cycles per stairs task, 10 gait cycles per ramp task, and 10 stand-sit cycles. At least five minutes of acclimation time was provided for each exoskeleton condition, and a five minute break was provided between conditions. Subjects were instructed not to use the handrails except to prevent a fall. A supplementary video of the experiments is available at [51].

Walking trials were separated into different tasks using a stopwatch and video recordings, and parsed into gait cycles by detecting heelstrike with a heel-mounted accelerometer. Stand-sit cycles were cropped into individual repetitions using an accelerometer built into the thigh-mounted EMG sensor. Each muscle's EMG was demeaned, bandpass filtered (20 - 200 Hz), smoothed with a moving 100 ms window RMS, and then normalized with respect to the maximum peak of the ensemble averages (across repetitions for each task/muscle) of all the active modes [52]. Hence, signals were converted to a percentage of the maximum voluntary contraction level (%MVC) for consistent comparison across subjects.

The subject-wise muscular efforts analysis involved a linear

mixed model (LMM) in MATLAB with restricted maximum likelihood estimation of parameters. Data from eight subjects were tabulated with information consisting of muscle effort change, exoskeleton condition (Bare, HipB, HipU, KneeB, KneeU), weight, LOA, and gender. We quantified muscular effort (%MVC.s) by integrating normalized EMG over time from the beginning to the end of five repeat trials for each exoskeleton condition [46]. We subtracted the %MVC.s of active conditions by the %MVC.s of the bare condition to determine the effort change. We defined exoskeleton conditions as categorical variables and fit a LMM, where the condition, weight, LOA, and gender are fixed effects:

Effort Change
$$\sim$$
 Controller + Weight + Gender + $(1|\text{Muscle}) + (1|\text{Task}) + (1|\text{Subject})$,

where $(1|\cdot)$ represents random effects. Statistical significance of each fixed effect parameter was determined by a two-tailed t-test. As a secondary analysis, a LMM without the random effects of task and muscle,

Effort Change
$$\sim$$
 Controller + Weight + Gender + $(1|Subject)$,

was applied to each muscle and task separately.

Though our goal was not to strictly reproduce biological human torque profiles, we analyzed the similarity between our applied torque and this biomechanical reference. We defined the cosine similarity metric (SIM) as $SIM(A,B) = 100 \cdot (A \cdot B)/(\|A\|_2 \|B\|_2)$ %. This similarity was then measured for each combination of exoskeleton condition and task, comparing the average human torque at the actuated joint (from the datasets [49], [50]) to the average applied torque (from our experiment). This metric was included to compare the behavior of the applied task-agnostic controller to a well-studied task-varying reference. We also calculated the average net work done per joint for each task and condition to investigate the generation of non-zero net work due to the power leak and passivity relaxation of the proposed control framework.

To quantify the controller's synchronization to the user, we additionally calculated the Pearson correlation coefficient between the EMG results and the applied exoskeleton joint torques. The formula of the coefficient for two vectors X, Y is

$$\rho_{X,Y} = \frac{\mathbf{E}[(X - \mu_X)(Y - \mu_y)]}{\sigma_x \sigma_y},$$

where μ_X, μ_Y are the mean values and σ_X, σ_Y are the standard deviations. The use of correlation helps account for the unknown offset between EMG and torque due to co-contraction.

Finally, we compared the kinematics of actuated joints between unilateral and bilateral conditions to identify any systematic behavioral changes between these configurations. We specifically examined overlaid phase plots of the actuated angles against the global thigh angle for each task.

IV. EXPERIMENTAL RESULTS

This section presents the experimental outcomes of our study. The bilateral knee condition of participants AB02 and AB03 were excluded due to a failure in the synchronization

between the left and right Raspberry Pi units. Moreover, the BF muscle's EMG data for participant AB04 were excluded because of a sensor failure, which was detected after the completion of the experiment.

A. Primary Analysis on Muscle Effort Change

Both of the unilateral configurations (KneeU and HipU) significantly reduced the muscular effort required to complete the activity circuit, with statistically significant fixed effects in our primary LMM (p < 0.001, Fig. 6). The HipU configuration reduced effort by an average of 2.71 %MVC.s, 95% confidence interval (CI) [1.16, 4.27]. The KneeU configuration reduced effort by 3.40 %MVC.s, 95% CI [1.85, 4.95]. There was also a significant gender effect, a penalty of 3.00 %MVC.s, 95% CI [0.46, 5.55] for women in all exoskeleton–bare comparisons (p = 0.021). This penalty is comparable in magnitude to the benefits from the unilateral controllers. Thus, there was only a net benefit for male subjects. A correlation was observed between weight and muscular effort, leading to an average reduction of $0.02 \cdot \text{mass}$ %MVC.s, 95% CI [-0.02, 0.06]. However, this correlation was not statistically significant, indicating that gender and weight were distinct effects.

The two bilateral configurations (KneeB and HipB) had a statistically null effect on muscular effort (p > 0.05). Considering the gender effect, this amounts to a net penalty for women. No significant effect was found for subject mass (p > 0.05). The kinematics indicated a slight reduction in global thigh angle range of motion for bilateral configurations as compared to unilateral configurations (Fig. 7).

B. EMG-Torque Correlation by Task

Correlation between extensor muscle activation and controller torque was high for the set of non-descent tasks (excluding SD and DD). As a baseline, normative biological profiles for hip and knee extension torque (from datasets [49], [50]) showed a modest to high correlation with our Baremode GLUT and VMO signals (Fig. 8, AB). The correlation between controller torque and these EMG measurements in the exoskeleton conditions (HipB, HipU, KneeB, KneeU) was task-dependent, but in several cases comparable. For the knee torque and VMO, the tasks of SA, LL, II, and SS were comparable to the baseline AB correlation. However, this correlation was markedly lower in SD and DD, the two decline tasks requiring negative work. Similarly, for the hip torque and GLUT, the tasks of SA, LL, II, and SS were of similar correlation to the baseline AB correlation, while the correlations in SD and DD tasks were even more clearly reduced, with an inverse correlation for the SD case.

C. EMG and Torque by Task and Condition

The across-subject muscle activation results for each task, configuration, and muscle offer a very detailed analysis of the controller's effect (Table II). Muscle effort comparisons were made between the bare mode and various exoskeleton configurations, where a positive value represents each muscle pair's effort increment (%MVC) with respect to the bare mode. These results can be interpreted through the measured control torques and ensemble-averaged VMO, RF, BF, and GLUT

EMGs for subject AB01 in Fig. 9 and Fig. 10. Furthermore the cosine similarity analysis in Table III indicates agreemen between exoskeleton torques and average human torques in most cases, noting the controller's goal was to deliver a weighted combination of biological and gravity compensation torques. Agreement was strongest for incline tasks and weakes for decline tasks (likely due to negative power tapering) Finally, the average net work analysis in Table IV shows the knee exoskeleton controllers provided net positive work for ascent tasks and net negative work for descent tasks, whereas the hip configurations only provided net positive work (note that AB hip work is also positive during descent tasks).

Incline walking and stair ascent are primarily associated with positive power via concentric muscle contractions in the quadriceps. The exoskeleton was able to facilitate clear reductions in the quadriceps (RF and VMO) EMG activation in stance phase (< 50% Cycle, see AB01 in Fig. 9). However, these quadriceps effort reductions in stair and ramp ascent tasks were highly variable across all subjects and device configurations, with bilateral configurations failing to achieve statistically significant reductions in particular (see Table II). Observations suggest that the subjects who were less familiar with the system struggled to anticipate the assistance of the devices and that the bilateral configurations interfered with natural motion more than the unilateral configurations. All configurations provided either knee or hip extension torques in the stance phase of these tasks, as expected. Unilateral hip modules (providing hip extension torques) were also capable of reducing GLUT EMG compared to the bare mode (see for AB01 in Fig. 9), however this effect was statistically insignificant across the participants (see Table II).

Stairs descent and decline walking are primarily associated with negative power and involve eccentric quadriceps contractions. Commonly, a double peak quadriceps activation profile occurs in stance; firstly to absorb the impact of heel strike, and secondly to lower the COM. However, due to the negative power tapering strategy, all active modes show a minor effect on EMG reductions compared to the bare mode. Both knee and hip modules provided minor knee and hip extension torques during early stance to absorb the impact.

Sit-to-stand and stand-to-sit primarily require knee extension torques [53], specifically concentric contractions during sit-to-stand and eccentric contractions during stand-to-sit. All knee modules provided substantial knee extension torques, resulting in a noticeable reduction in quadriceps activation (VMO and RF) for AB01 (see STS in Fig. 9). This effect appeared in the aggregate results across all subjects by the KneeU condition, with VMO and RF reduction (p < 0.01), while the effect was not replicated across the participants for the KneeB condition (see Table II). Hip modules also were capable of reducing quadriceps activation during sit-to-stand (see Fig. 9), however this effect was not detected by the secondary LMM analysis (see SS in Table II).

Knee flexors like the BF are responsible for lifting the foot in swing. Knee modules could be expected to assist with this flexion torque in level walking, however their reproduction of human-like flexion torques in this task was weak (see negative knee torque behavior for AB01 in Fig. 10). Across subjects, the

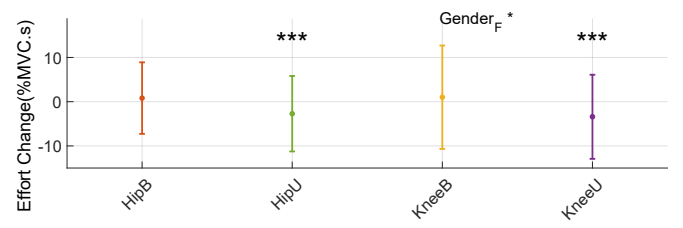


Fig. 6. Across-subject comparisons of total muscle effort during five repetitions. Combined muscle effort is compared between the bare mode and different exoskeleton configurations. A positive value represents the total muscle effort increment with respect to the bare mode. * represents statistical difference (p < 0.05), ** represents p <= 0.01, *** represents p <= 0.001.

controller was only able to reduce swing-phase BF activation using knee configurations in the ramp inline task (Table II). For this task, the controller appears to create a pulse of knee flexion in late-stance, agreeing with able-bodied torques in Fig. 10. The controller was also able to reduce BF activation in the SS task with the KneeU configuration, which is interesting since the predominant torque in SS is extension with notable co-contraction (see AB01's competing BF flexor and RF, and VMO extensor activation in late SS in Fig. 9).

The assistance torques provided by the hip modules are capable of reducing the hip extensor EMG (GLUT) for most of the tasks (see AB01, Fig. 9). This result was also not detectable in the population, with high variance in the EMG results (Table II). However, a GLUT EMG penalty with bilateral knee modules was significant in SA, SD, II (p < 0.001), and DD, LL (p < 0.01). Interestingly, the effect was much reduced for the unilateral condition of the knee exoskeleton (KneeU), with only a penalty in LL being significant (p < 0.01). In AB01, increased GLUT activation occurs in stance phase for the KneeB and KneeU conditions (Fig. 9).

V. DISCUSSION

The primary analysis revealed that the task-agnostic exoskeleton was notably beneficial in unilateral configurations with male users. However, there are three important caveats to this direct interpretation of the LMM's statistical test.

The first is the unintended correlation between acclimation experience and gender, which may partially explain the observed male-specific muscle effort reductions. Specifically, two male subjects (including AB01) were experienced and benefited significantly from the device. Experienced users can anticipate the exoskeleton's assistance behavior and utilize it effectively, while inexperienced users tend to co-contract muscles. Unfortunately, the amount of time needed for experiment setup, switching between different exoskeleton configurations, and trial repetitions made it impractical to provide more than 20 minutes of acclimation (across all tasks) per exoskeleton configuration, whereas [54] suggests that 30 minutes may be necessary for EMG reductions to occur (for a single task). Additionally, becoming an expert exoskeleton user typically requires substantial training, around 109 minutes for full adaptation [55]. We were unable to standardize acclimation across subjects and configurations, as the pilot subjects had more extensive acclimation. Based on our observations, it is likely that increased acclimation would enhance muscle activation benefits and mitigate the gender-related differences.

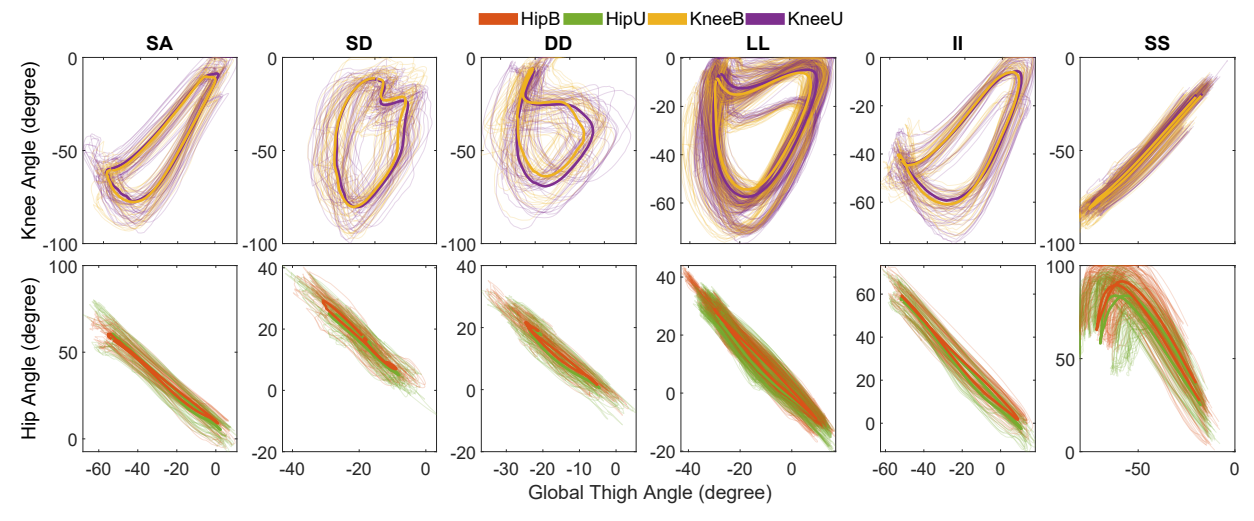


Fig. 7. Across-subject comparisons of the phase versus phase kinematics between the unilateral and bilateral modes for experiment tasks $\{\text{stair ascent/descent (6inch), decline/incline (12}^{\circ}), \text{ level ground, and stand-sit cycle}\}$. Thick solid lines represent the mean.

TABLE II ACROSS-SUBJECT COMPARISONS OF MUSCLE EFFORT CHANGE (MEAN \pm STANDARD DEVIATION IN %MVC.s) OVER DIFFERENT CASES.

		SA	SD	DD	LL	l II	SS
	KneeB	-3.27(15.02)	0.23(10.84)	-2.02(8.93)	4.63(2.83) ***	-2.97(9.69)	-16.87(26.67)
VMO	KneeU	-6.38(10.86)	-4.31(6.24)	-3.85(7)	2.08(2.32) *	-4.57(6.06)	-20.67(18.69) **
VIVIO	HipB	1(6.11)	1.54(6.18)	2.39(4.81)	2.16(2.33) *	-0.08(6.98)	6.19(18)
	HipU	-3.33(6.48)	-3.58(3.44)	-1.09(4.7)	0.22(2.47)	-3.47(6.62)	-7.17(17.44)
	KneeB	-1.27(7.69)	2.78(6.38)	-1.84(4.12)	4.01(3.17) **	-1.58(5.88)	-16.6(10.21)
RF	KneeU	-6.33(6.02) *	-6.6(4.61) **	-5.26(3.71) ***	1.13(1.06)	-4.98(5.09) *	-18.86(9.86) **
KI	HipB	-1.96(5.39)	-2.51(4.91)	0.08(3.95)	1.47(2.52)	-1.41(4.37)	1.12(18.05)
	HipU	-4.67(9.14)	-5.38(3.69) *	-2.58(3.19)	0.16(2.38)	-2.44(4.35)	-1.46(25.46)
	KneeB	4.17(10.37)	6.73(5.45) **	0.2(4.7)	2.22(9.41)	1.05(11.97)	-5.8(10.81)
BF	KneeU	-0.53(9.41)	-0.18(5.07)	-1.11(3.56)	-1.85(4.81)	-5.98(8.12) *	-10.65(12.04) *
DI.	HipB	1.45(7.05)	4.13(4.05) *	1.47(3.36)	1.42(2.43)	-1.36(10.64)	1.4(16.58)
	HipU	-1.54(8.36)	0.72(3.61)	-0.48(3.13)	1.01(1.48)	-7.61(7.01) *	-7.54(18.38)
	KneeB	17.73(7.53) ***	9.01(7.87) ***	3.79(3.46) **	5.41(3.7) **	10.15(5.5) ***	1.15(12.71)
GLUT	KneeU	3.15(6.52)	2.52(3.64)	1.43(2.25)	4.79(7.11) **	3.09(4.99)	-0.39(10.27)
GLUI	HipB	1.27(7.11)	0.49(3.73)	-0.79(2.62)	0.64(2.8)	0.37(7.31)	-2.05(13.67)
	HipU	-3.2(5.05)	-0.51(2.39)	-1.33(2.48)	-0.8(1.53)	-3.49(4.1)	-5.73(10.75)

A positive value represents the total muscle effort increment with respect to the bare mode. * represents statistical difference (p < 0.05), ** represents p <= 0.01.

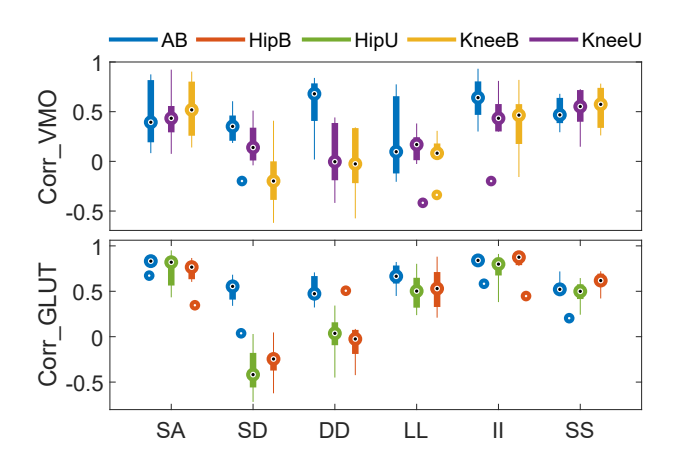


Fig. 8. Across-subject comparisons of the correlation coefficient between the EMG muscle activation and the applied joint torques for experiment tasks {stair ascent/descent (6inch), decline/incline (12°), level ground, stand-sit cycle} versus EMG Muscle Activation. The correlation coefficient between the EMG muscle activation (bare) and the normative AB human joint torques was calculated for illustration. Positive torques represent hip and knee extension. The overall significance of the correlation coefficients calculated by Fisher's method (meta-analysis) shows p < 0.05 across different experiment tasks.

TABLE III Subject 1 cosine similarity analysis (mean \pm standard deviation %).

	KneeB	KneeU	HipB	HipU
SA	83.8(14.0)	88.3(5.2)	72.6(5.9)	82.2(5.6)
SD	92.4(4.7)	93.9(3.2)	1.2(18.6)	6.9(7.9)
DD	75.1(7.0)	78.8(4.7)	-29.2(18.2)	-29.4(4.5)
LL	-4.7(27.5)	-0.5(14.9)	71.5(5.3)	63.3(16.5)
II	87.3(4.0)	79.0(11.2)	86.9(4.8)	87.6(4.8)
SS	70.8(13.6)	79.4(5.5)	80.1(10.7)	76.7(3.6)

TABLE IV Across-subject average net work per joint (mean \pm standard deviation in J/kg).

	KneeB	KneeU	HipB	HipU
SA	0.36(0.10)	0.39(0.11)	0.51(0.14)	0.44(0.13)
SD	-0.18(0.10)	-0.19(0.12)	0.00(0.05)	0.04(0.06)
DD	-0.16(0.08)	-0.16(0.11)	0.11(0.06)	0.11(0.05)
LL	0.07(0.07)	0.12(0.07)	0.25(0.13)	0.24(0.12)
II	0.25(0.13)	0.33(0.16)	0.66(0.25)	0.59(0.25)
SS	0.21(0.08)	0.26(0.08)	0.67(0.23)	0.64(0.20)

Torques are normalized by LOA% and body weight.

Second, the smallest size of the off-the-shelf hip braces was notably uncomfortable for the shortest participants, which may have disproportionately affected women compared to men. This may have led to the 2.65% MVC.s increase in muscle

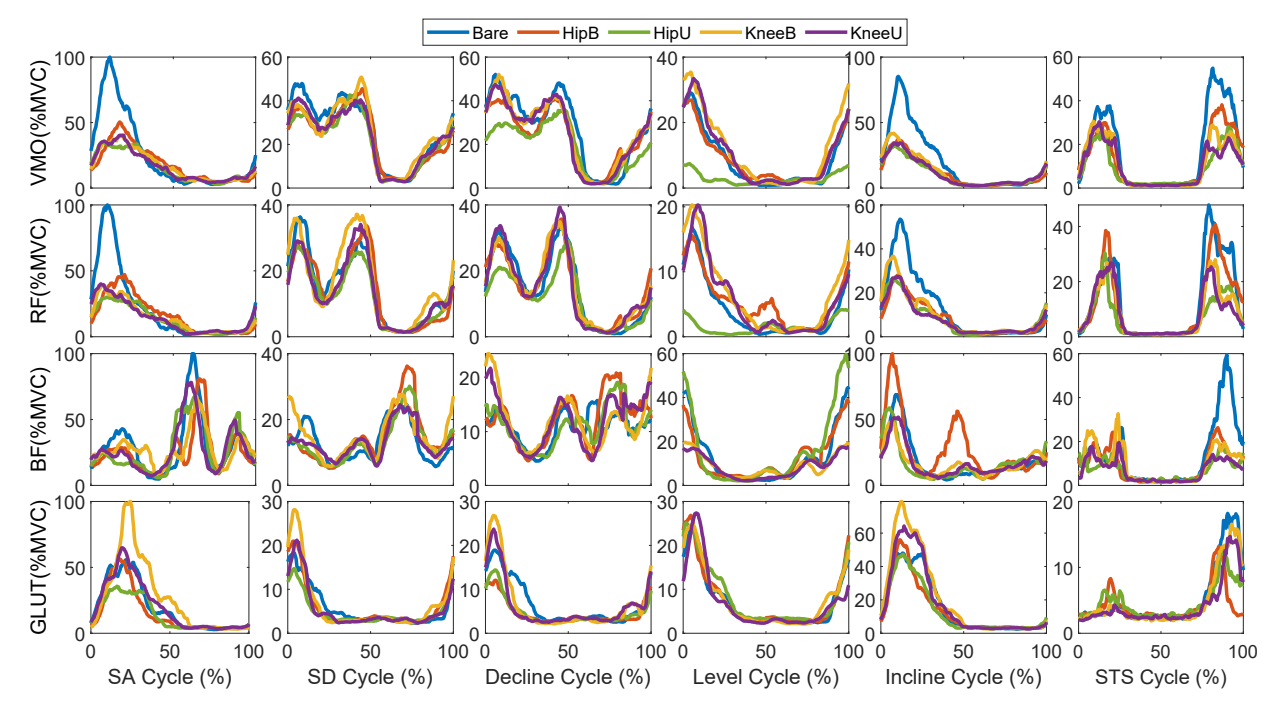


Fig. 9. Subject 1 EMG comparisons between bare and different exoskeleton configurations for each muscle (VMO, RF, BF, and GLUT) and task {stair ascent/descent (6inch), decline/incline (12°), level ground, and sit-stand cycle}. Results are time-normalized ensemble averages across all repetitions.

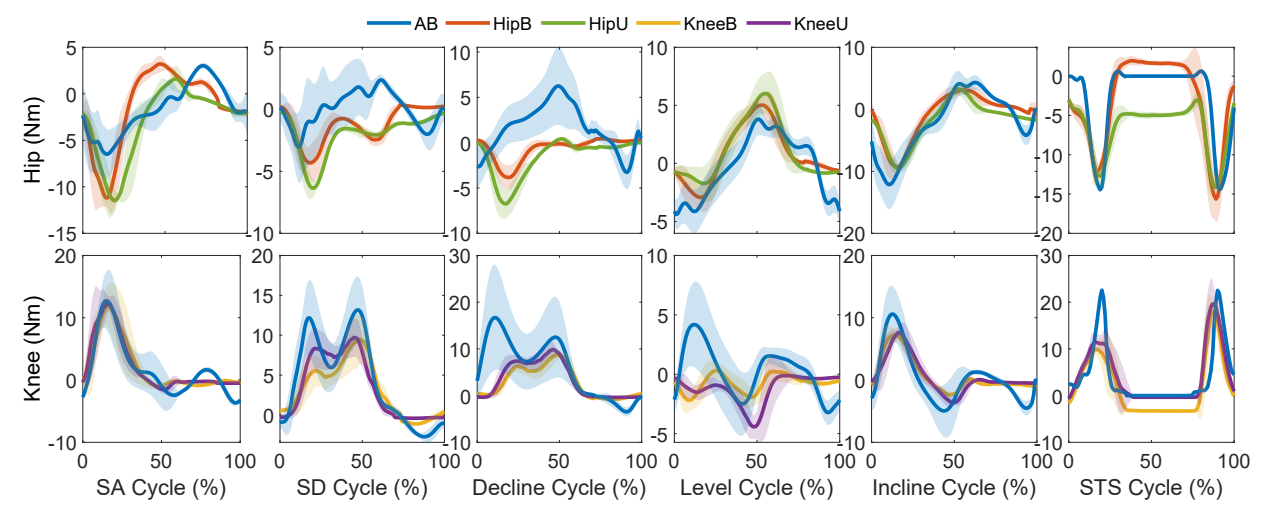


Fig. 10. Subject 1 averaged command torques for experiment tasks {stair ascent/descent (6inch), decline/incline (12°), level ground, stand-sit cycle}. The red (HipB), green (HipU), yellow (KneeB), and purple (KneeU) lines represent the mean exoskeleton torque across all repetitions for the active modes. Normative AB joint torques from [49], [50] (blue lines) have been scaled by LOA% for better comparison. Positive torques represent hip flexion and knee extension.

effort for women in bilateral hip configurations compared to a 1.15% MVC.s decrease in muscle effort for men. Moreover, this discomfort likely influenced female participants' inclination toward lower LOA% values during the tuning process, which influenced their peak assistance torque. The overall LOA% for female subjects was 26.47% lower in knee configurations and 43.48% lower in hip configurations compared to male subjects. This notable gender-based divergence could potentially explain the distinct muscle effort reductions observed for males vs. females.

The third caveat pertains to the unmeasured physical effect of wearing bilateral configurations, which impede out-of-plane motion and add mass. Specifically, the bilateral configurations introduced an additional mass of 1.9 kg for the knee exoskeletons and 1.7 kg for the hip exoskeletons, as compared to their unilateral counterparts. The notable increase in GLUT muscle effort in SA when using KneeB, but not when using KneeU, may be attributed to the additional mass of the contralateral leg when it is swinging during gait. While the command torques were similar between bilateral and unilateral conditions for the same joints, the observed penalties in muscle activation, whether direct or indirect, may also be attributed to the form factor of the device. Participants informally reported that their motion was notably physically constrained when using the bilateral configurations. Fig. 7 highlights subtle kinematic differences between unilateral and bilateral modes, including

a 26.66% reduction in range of motion for the hip joint and an 11.33% reduction for the knee joint in bilateral configurations compared to the unilateral ones. These variations in kinematics can influence muscle activation patterns and result in varying muscle effort levels. Considering these limitations, it is possible that a direct interpretation of the primary analysis may underestimate the controller's benefits, motivating future studies with more comfortable and adjustable hardware. In fact, a related controller implemented on revised bilateral knee modules successfully reduced quadriceps and hamstrings EMG effort without a gender penalty [56].

The detailed secondary analyses show the control method produced helpful torque outputs across tasks and configurations of the device. Among all the active modes, the unilateral hip module produced the greatest EMG reductions among all tasks for AB01 as shown in Fig. 9, but muscle effort reduction was different for each subject over the various *M-BLUE* configurations. The benefits of the unilateral configurations on RF and VMO were clear in several tasks. Only AB02, AB03, and AB04 had greater reductions in muscle efforts in the bilateral cases over the unilateral cases. This discrepancy may depend on how subjects acclimate to the various configurations.

During sit-to-stand, we found large reductions in VMO (knee extensor) and BF (hip extensor) activations with the unilateral knee exoskeleton configuration when compared to bare mode (see Table II for mean effort changes). The reductions in VMO and GLUT activations were also aligned with the exoskeleton assistance torques, as shown in Fig. 8. Although KneeU and KneeB provided no direct hip assistance torque, we found a reduction in BF activation, which can be due to a change of strategy to a more knee-dominant one.

Stair and ramp climbing during stance have similar biomechanics to sit-to-stand, whereby knee extension and hip extension torques are required during early to mid stance to elevate the body's center of mass [57]. Accordingly, we found reductions in VMO and RF activations during early to mid stance (see Fig. 9 for ensembled EMG averages). The correlation between dominant muscle EMG and torque profiles in Fig. 8 shows a harmony of the assistive torques with the nervous system in stair ascent and incline walking. Overall, reductions in muscle activation aligned with the respective assistance torque, showing the contribution of *M-BLUE* towards the net joint torque. This was made possible by relaxing passivity with power leak terms (Section II-D) to allow net positive or negative work over the gait cycle (Table IV).

The above-mentioned results could have been positively or negatively impacted by insufficient experimental control over kinematic variability between bare and exoskeleton conditions. Although the study design aimed to strike a balance between practicality and experimental control, such as averaging several repeat trials to reduce noise, there were unanticipated aspects of the user experience that may have affected the results. Specifically, introducing the exoskeleton and its torque may have influenced the kinematics/kinetics of subjects, potentially altering EMG signals. For example, subjects may have unconsciously changed their gait style, shifting their load from the knees to hips or vice versa to leverage (or fight) the assistance. In subsequent pilot testing, we found that stricter

enforcement of gait style leads to a clearer exoskeleton effect on muscle effort, suggesting this effect may have been hidden by kinematic/kinetic variation between conditions in this study. The observed low peak torque values during ascent tasks may have contributed to weak EMG trends. To safeguard the actuator, we limited the torque to 25 Nm, although this level was never reached during ascent tasks. For example, Fig. 10 illustrates that a torque of around 10 Nm during ascent tasks led to EMG reduction trends in subject AB01.

Our tests have only covered a subset of the exoskeleton configurations that are possible in our control framework. While this paper considered knee and hip joints separately, the combination of knee and hip joints would introduce even more predictive power into the basis function set. In fact, the framework can be deployed to arbitrary uni- or bi-lateral ankle, knee, and/or hip configurations of M-BLUE. It could even extend beyond this, to joints out of the sagittal plane like the frontal plane hip abduction/adduction torque. However, the success of these unproven cases will depend on the available sensor signals being sufficiently distinct between tasks to generate a unique mapping from these signals to task-specific joint torques. It is also worth noting that the presented controller can be readily applied to populations with gait kinematics within our training data distribution, such as elderly individuals. Future work will consider extending this framework to diverse patient populations by including population-specific data in the optimization, enabling applications in rehabilitation.

VI. CONCLUSION

This paper presented a modular solution for task-agnostic control of a broad class of exoskeletons to assist broad patient populations in their activities of daily living. The Modular Multi-Task Optimal Energy Shaping control framework generates controllers for various configurations of active joints that optimally account for multiple tasks in human biomechanical data. A human trial with N=8 able-bodied participants demonstrated the potential benefits of the modular exoskeleton controllers to reduce muscle effort, while identifying remaining challenges to be resolved in future work.

ACKNOWLEDGMENTS

The authors thank Avani Yerva, Christopher Nesler, Hannah Frame, Qinyi Zhou, and Elliott J. Rouse for their assistance.

APPENDIX

The motor safety strategy ran a real-time simulation of the winding temperature, based on an offline system identification experiment and a simple model with two temperature states (see Fig. 11), resulting in an ODE model of the form

$$\dot{T}_{w} = \frac{I_{q}^{2} R_{q}}{C_{w}} + \frac{T_{h} - T_{w}}{R_{w-h} C_{w}}, \quad \dot{T}_{h} = \frac{T_{w} - T_{h}}{R_{w-h} C_{h}} + \frac{T_{a} - T_{h}}{R_{h-a} C_{h}}, \quad (17)$$

where $I_q^2 R_q$ is the joule heating of the motor windings, the temperatures of the winding, housing, and ambient are denoted T_w , T_h , and T_a , respectively, and the resistive and capacitive thermal circuit elements are laid out as diagrammed in Fig. 11.b. This temperature safety system was used in place

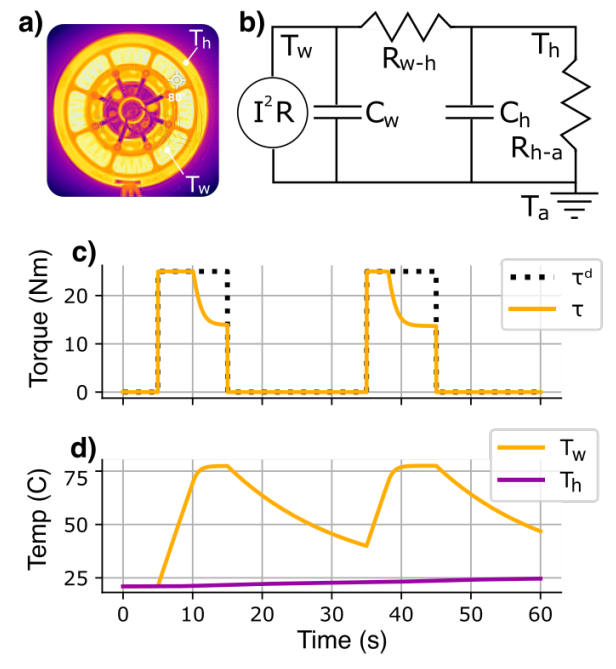


Fig. 11. **Model-based thermal limits** were identified using the dynamics of the winding temperature T_w and case temperature T_c in thermal images (a) and fit to a thermal circuit model (b), which allowed development of a safety controller that reduces desired torque (c) in order to provide strict guarantees on the maximum temperatures (d). Continuous torque of 8.76 Nm only occurs after the housing reaches 58 degrees, whereas the torque is limited closer to 13.7 Nm in (c) due to high winding temperature with a cool housing.

of the conservative safety limits of the ActPacks by installing custom firmware without the default I^2R safety limits.

To ensure the temperature limits are not breached for any desired q-axis current, I_q^d , we define the true current I_q as

$$I_q = \sqrt{S_{\tilde{\sigma}_h}^{\tilde{\sigma}_h}(T_h)S_{\tilde{\sigma}_w}^{\tilde{\sigma}_w}(T_w)}I_q^d, \tag{18}$$

in terms of the following soft-limiting function:

$$S_{\tilde{\sigma}}^{\tilde{\sigma}}(T) = \begin{cases} 1 & T \leq \tilde{\sigma} \\ \frac{\tilde{\sigma} - T}{\tilde{\sigma} - \tilde{\sigma}} & \tilde{\sigma} < T < \tilde{\sigma} \\ 0 & T \geq \tilde{\sigma} \end{cases}$$
 (19)

This law provides a formal safety guarantee while also avoiding sudden shut-offs of power to the device.

Lemma A.1. The set of safe temperatures,

$$\mathscr{T} = \{ (T_h, T_w) \mid T_a \le T_h \le \bar{\sigma}_h, \ T_a \le T_w \le \bar{\sigma}_w \},$$

is invariant under any control law that satisfies $T_w = \bar{\sigma}_w \Longrightarrow I_q = 0$ (including the proposed temperature safety control law), so long as $T_a \le \bar{\sigma}_h \le \bar{\sigma}_w$ and $\bar{\sigma}_w - \bar{\sigma}_h \le \frac{R_{w-h}}{R_{h-a}}(\bar{\sigma}_h - T_a)$.

Proof. Consider the four edges of this rectangular set. At the edge $T_w = T_a$, $(T_h, T_w) \in \mathcal{T}$ implies that the two terms in \dot{T}_w (17) are non-negative, so the state cannot escape \mathcal{T} by passing through this edge. Similarly, at the edge $T_h = T_a$, $(T_h, T_w) \in \mathcal{T}$ implies that the first term in \dot{T}_h (17) is non-negative and the second is zero, again prohibiting escape. At the edge $T_w = \bar{\sigma}_w$, $(T_h, T_w) \in \mathcal{T}$ implies

$$\dot{T}_{w}\big|_{T_{w}=\bar{\sigma}_{w}} = \frac{I_{q}^{2}K_{q}^{*0}}{C_{w}} + \frac{T_{h}-\bar{\sigma}_{w}}{R_{w-h}C_{w}} \le \frac{\bar{\sigma}_{h}-\bar{\sigma}_{w}}{R_{w-h}C_{w}} \le 0.$$
 (20)

And at the remaining edge $T_h = \bar{\sigma}_h$, $(T_h, T_w) \in \mathcal{T}$ implies

$$\begin{aligned}
|\dot{T}_{h}|_{T_{h} = \bar{\sigma}_{h}} &= \frac{T_{w} - \bar{\sigma}_{h}}{R_{w-h}C_{h}} + \frac{T_{a} - \bar{\sigma}_{h}}{R_{h-a}C_{h}} \leq \frac{\bar{\sigma}_{w} - \bar{\sigma}_{h}}{R_{w-h}C_{h}} + \frac{T_{a} - \bar{\sigma}_{h}}{R_{h-a}C_{h}} \\
&\leq \frac{\bar{\sigma}_{h} - T_{a}}{R_{h-a}C_{h}} + \frac{T_{a} - \bar{\sigma}_{h}}{R_{h-a}C_{h}} = 0.
\end{aligned} (21)$$

Thus, since the state of the system cannot escape any boundary of \mathscr{T} , \mathscr{T} is an invariant set.

In practice, this means that we can guarantee the upper winding temperature limit, $\bar{\sigma}_w$, (80 C) and the upper housing temperature limit, $\bar{\sigma}_h$, (70 C) are never breached without any knowledge of rest of the controller or human actions. The soft limits at $\tilde{\sigma}_w = 70$ C and $\tilde{\sigma}_h = 60$ C soften the loss of torque when we get to the temperature limits (Fig. 11.c-d demonstrates this behavior in simulation). In practice, the housing temperature is relatively low in our experiments, due to the breaks we provide the subjects. We used a temperature sensor on the actuator module's logic board to provide an estimate for T_h , which we used in place of the simulation estimate of this value for the purposes of limiting current, since this is more reliable in the event of a software restart.

REFERENCES

- [1] G. Zeilig, H. Weingarden, M. Zwecker, I. Dudkiewicz, A. Bloch, and A. Esquenazi, "Safety and tolerance of the rewalk™ exoskeleton suit for ambulation by people with complete spinal cord injury: a pilot study," J. Spinal Cord Med., vol. 35, no. 2, pp. 96–101, 2012.
- [2] O. Harib, A. Hereid, A. Agrawal, T. Gurriet, S. Finet, G. Boeris, A. Duburcq, M. E. Mungai, M. Masselin, A. D. Ames *et al.*, "Feedback control of an exoskeleton for paraplegics: Toward robustly stable, handsfree dynamic walking," *IEEE Control Syst. Mag.*, vol. 38, no. 6, pp. 61–87, 2018.
- [3] T. Yan, M. Cempini, C. M. Oddo, and N. Vitiello, "Review of assistive strategies in powered lower-limb orthoses and exoskeletons," *Robot. Auton. Syst.*, vol. 64, pp. 120–136, 2015.
- [4] R. Baud, A. R. Manzoori, A. Ijspeert, and M. Bouri, "Review of control strategies for lower-limb exoskeletons to assist gait," *J. Neuroeng. Rehabil.*, vol. 18, no. 1, pp. 1–34, 2021.
- [5] B. Laschowski and J. McPhee, "Energy-efficient actuator design principles for robotic leg prostheses and exoskeletons: A review of series elasticity and backdrivability," *J. Comput. Nonlinear Dyn.*, vol. 18, no. 6, p. 060801, 2023.
- [6] G. Lv, H. Zhu, and R. D. Gregg, "On the design and control of highly backdrivable lower-limb exoskeletons: A discussion of past and ongoing work," *IEEE Control Syst. Mag.*, vol. 38, no. 6, pp. 88–113, 2018.
- [7] H. Zhu, C. Nesler, N. Divekar, V. Peddinti, and R. Gregg, "Design principles for compact, backdrivable actuation in partial-assist powered knee orthoses," *IEEE/ASME Trans. Mechatron.*, vol. 26, no. 6, pp. 3104– 3115, 2021.
- [8] S. Yu, T.-H. Huang, X. Yang, C. Jiao, J. Yang, Y. Chen, J. Yi, and H. Su, "Quasi-direct drive actuation for a lightweight hip exoskeleton with high backdrivability and high bandwidth," *IEEE/ASME Trans. Mechatron.*, vol. 25, no. 4, pp. 1794–1802, 2020.
- [9] T.-H. Huang, S. Zhang, S. Yu, M. K. MacLean, J. Zhu, A. Di Lallo, C. Jiao, T. C. Bulea, M. Zheng, and H. Su, "Modeling and stiffnessbased continuous torque control of lightweight quasi-direct-drive knee exoskeletons for versatile walking assistance," *IEEE Trans. Robot.*, vol. 38, no. 3, pp. 1442–1459, 2022.
- [10] C. Nesler, G. Thomas, N. Divekar, E. J. Rouse, and R. D. Gregg, "Enhancing voluntary motion with modular, backdrivable, powered hip and knee orthoses," *IEEE Robot. Autom. Lett.*, vol. 7, no. 3, pp. 6155– 6162, 2022.
- [11] F. Giovacchini, F. Vannetti, M. Fantozzi, M. Cempini, M. Cortese, A. Parri, T. Yan, D. Lefeber, and N. Vitiello, "A light-weight active orthosis for hip movement assistance," *Robot. Auton. Syst.*, vol. 73, pp. 123–134, 2015.
- [12] T. Zhang, M. Tran, and H. Huang, "Design and experimental verification of hip exoskeleton with balance capacities for walking assistance," *IEEE/ASME Trans. Mechatron.*, vol. 23, no. 1, pp. 274–285, 2018.

- [13] S. V. Sarkisian, M. K. Ishmael, G. R. Hunt, and T. Lenzi, "Design, development, and validation of a self-aligning mechanism for high-torque powered knee exoskeletons," *IEEE Trans. Med. Robot. Bionics*, vol. 2, no. 2, pp. 248–259, 2020.
- [14] I. Kang, R. R. Peterson, K. R. Herrin, A. Mazumdar, and A. J. Young, "Design and validation of a torque-controllable series elastic actuator-based hip exoskeleton for dynamic locomotion," *J. Mech. Robot.*, vol. 15, no. 2, p. 021007, 2023.
- [15] U. Nagarajan, G. Aguirre-Ollinger, and A. Goswami, "Integral admittance shaping: A unified framework for active exoskeleton control," *Robot. Auton. Syst.*, vol. 75, pp. 310–324, 2016.
- [16] G. Aguirre-Ollinger, J. E. Colgate, M. A. Peshkin, and A. Goswami, "Inertia compensation control of a one-degree-of-freedom exoskeleton for lower-limb assistance: Initial experiments," *IEEE Trans. Neural Syst. Rehabil. Eng.*, vol. 20, no. 1, pp. 68–77, 2012.
- [17] S. A. Murray, K. H. Ha, C. Hartigan, and M. Goldfarb, "An assistive control approach for a lower-limb exoskeleton to facilitate recovery of walking following stroke," *IEEE Trans. Neural Syst. Rehabil. Eng.*, vol. 23, no. 3, pp. 441–449, 2014.
- [18] G. C. Thomas, O. Campbell, N. Nichols, N. Brissonneau, B. He, J. James, N. Paine, and L. Sentis, "Formulating and deploying strength amplification controllers for lower-body walking exoskeletons," *Front. Robot. AI*, vol. 8, p. 295, 2021.
- [19] C.-Y. Kuo, D.-Y. Wu, and C.-Y. Lin, "Rnn based knee joint muscular torque estimation of a knee exoskeleton for stair climbing," in *IEEE Int. Conf. Mechatron. Technol.*, 2021, pp. 1–6.
- [20] D. D. Molinaro, I. Kang, and A. J. Young, "Estimating human joint moments unifies exoskeleton control, reducing user effort," *Science Robotics*, vol. 9, no. 88, p. eadi8852, 2024.
- [21] A. Ancillao, S. Tedesco, J. Barton, and B. O'Flynn, "Indirect measurement of ground reaction forces and moments by means of wearable inertial sensors: A systematic review," *Sensors*, vol. 18, no. 8, p. 2564, 2018.
- [22] I. Kang, P. Kunapuli, and A. J. Young, "Real-time neural network-based gait phase estimation using a robotic hip exoskeleton," *IEEE Trans. Med. Robot. Bionics*, vol. 2, no. 1, pp. 28–37, 2019.
- [23] K. Seo, Y. J. Park, J. Lee, S. Hyung, M. Lee, J. Kim, H. Choi, and Y. Shim, "Rnn-based on-line continuous gait phase estimation from shank-mounted imus to control ankle exoskeletons," in *IEEE Int. Conf. Rehabil. Robot.*, 2019, pp. 809–815.
- [24] I. Kang, D. D. Molinaro, G. Choi, J. Camargo, and A. J. Young, "Subject-independent continuous locomotion mode classification for robotic hip exoskeleton applications," *IEEE. Trans. Biomed. Eng.*, vol. 69, no. 10, pp. 3234–3242, 2022.
- [25] D. Y. Li, A. Becker, K. A. Shorter, T. Bretl, and E. T. Hsiao-Wecksler, "Estimating system state during human walking with a powered anklefoot orthosis," *IEEE/ASME Trans. Mechatron.*, vol. 16, no. 5, pp. 835– 844, 2011.
- [26] R. L. Medrano, G. C. Thomas, C. G. Keais, E. J. Rouse, and R. D. Gregg, "Real-time gait phase and task estimation for controlling a powered ankle exoskeleton on extremely uneven terrain," *IEEE Trans. Robot.*, vol. 39, no. 3, pp. 2170–2182, 2023.
- [27] R. Ronsse, N. Vitiello, T. Lenzi, J. Van Den Kieboom, M. C. Carrozza, and A. J. Ijspeert, "Human–robot synchrony: flexible assistance using adaptive oscillators," *IEEE. Trans. Biomed. Eng.*, vol. 58, no. 4, pp. 1001–1012, 2010.
- [28] M. K. Ishmael, D. Archangeli, and T. Lenzi, "Powered hip exoskeleton improves walking economy in individuals with above-knee amputation," *Nat. Med.*, vol. 27, no. 10, pp. 1783–1788, 2021.
- [29] M. S. Orendurff, J. A. Schoen, G. C. Bernatz, A. D. Segal, and G. K. Klute, "How humans walk: bout duration, steps per bout, and rest duration." J. Rehabil. Res. Dev., vol. 45, no. 7, 2008.
- [30] A. M. Bloch, N. E. Leonard, and J. E. Marsden, "Stabilization of mechanical systems using controlled lagrangians," in *IEEE Conf. Decis. Control*, vol. 3, 1997, pp. 2356–2361.
- [31] R. Ortega, A. Loría, P. J. Nicklasson, and H. J. Sira-Ramirez, Passivitybased control of Euler-Lagrange systems. Springer-Verlag, 1998.
- [32] J. Lin, N. V. Divekar, G. Lv, and R. D. Gregg, "Optimal task-invariant energetic control for a knee-ankle exoskeleton," *IEEE Control Syst. Lett.*, vol. 5, no. 5, pp. 1711–1716, 2020.
- [33] J. Lin, N. V. Divekar, G. C. Thomas, and R. D. Gregg, "Optimally biomimetic passivity-based control of a lower-limb exoskeleton over the primary activities of daily life," *IEEE Open J. Control Syst.*, vol. 1, pp. 15–28, 2022.
- [34] G. Lv, H. Zhu, T. Elery, L. Li, and R. D. Gregg, "Experimental implementation of underactuated potential energy shaping on a powered

- ankle-foot orthosis," in *IEEE Int. Conf. Robot. Autom.*, 2016, pp. 3493–3500.
- [35] G. Lv and R. D. Gregg, "Underactuated potential energy shaping with contact constraints: Application to a powered knee-ankle orthosis," *IEEE Trans. Control Syst. Technol.*, vol. 26, no. 1, pp. 181–193, 2018.
- [36] J. Lin, G. Lv, and R. D. Gregg, "Contact-invariant total energy shaping control for powered exoskeletons," in *American Control Conf.* IEEE, 2019, pp. 664–670.
- [37] G. C. Thomas and R. D. Gregg, "An energy shaping exoskeleton controller for human strength amplification," in *IEEE Conf. Decis.* Control. IEEE, 2021, pp. 1419–1425.
- [38] J. Zhang, J. Lin, V. Peddinti, and R. D. Gregg, "Optimal energy shaping control for a backdrivable hip exoskeleton," in *American Control Conf.* IEEE, 2023.
- [39] R. Ortega, A. Van Der Schaft, B. Maschke, and G. Escobar, "Interconnection and damping assignment passivity-based control of portcontrolled hamiltonian systems," *Automatica*, vol. 38, no. 4, pp. 585– 596, 2002
- [40] R. Ortega, A. J. Van Der Schaft, I. Mareels, and B. Maschke, "Putting energy back in control," *IEEE Control Syst. Mag.*, vol. 21, no. 2, pp. 18–33, 2001.
- [41] J. Pratt, C.-M. Chew, A. Torres, P. Dilworth, and G. Pratt, "Virtual model control: An intuitive approach for bipedal locomotion," *Int. J. Robot. Res.*, vol. 20, no. 2, pp. 129–143, 2001.
- [42] J. J. Craig, Introduction to Robotics. Addison-Wesley Publishing Company, 1986.
- [43] M. James, "The generalised inverse," The Mathematical Gazette, vol. 62, no. 420, pp. 109–114, 1978.
- [44] D. J. Braun and M. Goldfarb, "A control approach for actuated dynamic walking in biped robots," *IEEE Trans. Robot.*, vol. 25, no. 6, pp. 1292– 1303, 2009.
- [45] H. K. Khalil, Nonlinear systems. Upper Saddle River, NJ: Prentice Hall, 2002, vol. 3.
- [46] N. Divekar, J. Lin, C. Nesler, S. Borboa, and R. D. Gregg, "A potential energy shaping controller with ground reaction force feedback for a multi-activity knee-ankle exoskeleton," in *IEEE Int. Conf. Biomed. Robot. Biomechatron.*, 2020.
- [47] M. Grant and S. Boyd, "CVX: Matlab software for disciplined convex programming, version 2.1," http://cvxr.com/cvx, Mar. 2014.
- [48] M. Grant, S. Boyd, and Y. Ye, "Disciplined convex programming," in Global optimization. Springer, 2006, pp. 155–210.
- [49] J. Camargo, A. Ramanathan, W. Flanagan, and A. Young, "A comprehensive, open-source dataset of lower limb biomechanics in multiple conditions of stairs, ramps, and level-ground ambulation and transitions," *J. Biomech.*, vol. 119, p. 110320, 2021.
- [50] B. Laschowski, R. S. Razavian, and J. McPhee, "Simulation of stand-to-sit biomechanics for robotic exoskeletons and prostheses with energy regeneration," *IEEE Trans. Med. Robot. Bionics*, vol. 3, no. 2, pp. 455–462, 2021.
- [51] J. Lin, G. C. Thomas, N. V. Divekar, V. Peddinti, and R. D. Gregg, "Modular lower-limb exoskeleton assisting the activities of daily life," https://youtu.be/xuD56DZpbvI, 2023.
- [52] J. F. Yang and D. Winter, "Electromyographic amplitude normalization methods: improving their sensitivity as diagnostic tools in gait analysis." *Arch. Phys. Med. Rehabil.*, vol. 65, no. 9, pp. 517–521, 1984.
- [53] P. J. Millington, B. M. Myklebust, and G. M. Shambes, "Biomechanical analysis of the sit-to-stand motion in elderly persons," *Arch. Phys. Med. Rehabil.*, vol. 73, no. 7, pp. 609–617, 1992.
- [54] T. Lenzi, M. C. Carrozza, and S. K. Agrawal, "Powered hip exoskeletons can reduce the user's hip and ankle muscle activations during walking," *IEEE Trans. Neural Syst. Rehabil. Eng.*, vol. 21, no. 6, pp. 938–948, 2013
- [55] K. L. Poggensee and S. H. Collins, "How adaptation, training, and customization contribute to benefits from exoskeleton assistance," *Sci. Robot.*, vol. 6, no. 58, p. eabf1078, 2021.
- [56] N. Divekar, "Task-invariant control and pre-clinical validation of partial assist exoskeletons," Ph.D. dissertation, University of Michigan, 2023.
- [57] S. Nadeau, B. J. McFadyen, and F. Malouin, "Frontal and sagittal plane analyses of the stair climbing task in healthy adults aged over 40 years: what are the challenges compared to level walking?" Clin. Biomech., vol. 18, no. 10, pp. 950–959, 2003.



Jianping Lin (Member, IEEE) received the B.S. degree in applied mathematics from East China Normal University, Shanghai, China, in 2012, the M.S. degree in mechanical engineering from The University of Texas at Dallas, Richardson, TX, USA, in 2015, and the M.S. and Ph.D. degrees in robotics from the University of Michigan, Ann Arbor, MI, USA, in 2020 and 2021, respectively. He is currently a Research Fellow at the School of Mechanical Engineering, Shanghai Jiao Tong University, Shanghai, China. His research interests include the design and

control of wearable devices and robots.



Robert D. Gregg (Senior Member, IEEE) received the B.S. degree in electrical engineering and computer sciences from the University of California at Berkeley, Berkeley, CA, USA, in 2006, and the M.S. and Ph.D. degrees in electrical and computer engineering from the University of Illinois at Urbana-Champaign, Champaign, IL, USA, in 2007 and 2010, respectively. He was previously an Assistant Professor with The University of Texas at Dallas, Richardson, TX, USA. In 2019, he became an Associate Professor of the Department of Electrical

Engineering and Computer Science at the University of Michigan, Ann Arbor, MI, USA, where he joined the Department of Robotics in 2022. His research interests include the control of bipedal locomotion with applications to autonomous and wearable robots.



Gray C. Thomas (Member, IEEE) received the B.S. degree in general engineering with a self-designed concentration in robotics at Olin College of Engineering, Needham, MA, USA, in 2012, and the Ph.D. degree in Mechanical Engineering from the University of Texas at Austin, Austin, TX, USA, in 2019. He was previously a Research Investigator with the University of Michigan, Ann Arbor, TX, USA. In 2023, he became an Assistant Professor in the J. Mike Walker '66 Department of Mechanical Engineering at Texas A&M University, College

Station, TX, USA, where he directs the Human-Empowering Robotics and Control (HERC) Lab. His research interests include control and control-oriented design of physically-interactive robots as well as modeling and estimation of humans.



Nikhil V. Divekar (Member, IEEE) received his B.S. degree in Mechatronics Engineering (University of Cape Town, 2008), M.S. degree in Biomedical Engineering (University of Cape Town, 2013), M.S. degree in Bioengineering (University of Texas at Dallas, 2020), M.S. degree in Robotics (University of Michigan - Ann Arbor, 2021), PhD degree in Robotics (University of Michigan - Ann Arbor, 2023). He is currently working as a Postdoctoral Research Fellow at the Department of Robotics, University of Michigan - Ann Arbor. His research

interests include biomechanics, neurophysiology, and control of wearable robots.



Vamsi Peddinti received the B.S. degree in electronics and computer engineering from the Gandhi Institute of Technology and Management, Visakhapatnam, India, and the M.S. degree in electrical and electronics engineering from the Indiana University—Purdue University Indianapolis, Indianapolis, IN, USA, in 2015 and 2018, respectively. He was previously a Research Engineer with the University of Michigan, Ann Arbor, MI, USA. He is currently a Senior Systems Engineer with Micron Technology, Hyderabad, TS, India, where he works on various

memory storage devices and their affiliated products.